

A search for charged Higgs boson with the ATLAS detector at the LHC

Dissertation submitted in partial fulfillment of the requirements of the degree of M.Sc. in the Bverley and Raymond School of Physics and Astronomy at Tel Aviv University under the supervision of Prof. Erez Etzion

HADAR COHEN

OCTOBER 5, 2016

CERN-THESIS-2016-187
30/11/2016



TEL AVIV אוניברסיטת
UNIVERSITY תל אביב

Contents

1	Introduction	7
2	Theoretical background	9
2.1	The Standard Model of particle physics	9
2.1.1	Particles of the Standard Model	9
2.1.2	Gauge theory of weak interactions	12
2.1.3	Spontaneous symmetry breaking and the Higgs mechanism	14
2.2	Beyond the Standard Model (BSM) physics	18
2.2.1	Phenomena not explained by the Standard Model	19
2.2.2	The charged Higgs boson	20
3	The CERN laboratory	24
3.1	The accelerator infrastructure	25
3.1.1	Linear accelerators	25
3.1.2	Proton Synchrotron Booster (PSB)	27
3.1.3	Proton Synchrotron (PS)	27
3.1.4	Super Proton Synchrotron (SPS)	27

3.2	The Large Hadron Collider (LHC)	28
3.3	LHC experiments	29
4	The ATLAS detector system	31
4.1	Overview	31
4.2	Conventions	33
4.3	Inner detector	34
4.4	Calorimeters	37
4.5	Muon spectrometer	39
4.6	Trigger system	42
5	Charged Higgs boson search in ATLAS	44
5.1	Production and decay of charged Higgs boson	44
5.2	Data and simulation samples	46
5.2.1	Data samples	46
5.2.2	Monte Carlo simulations	47
5.3	Event Selection	50
5.3.1	Objects reconstruction	51
5.3.2	Charged Higgs boson selection	56
5.4	Backgrounds	58
5.4.1	$t\bar{t}$ heavy flavour classification	58
5.4.2	Background composition	59
5.5	Signal and background separation using Boosted Decision Trees	61
5.5.1	Decision trees and boosting	61

5.5.2	Input variables	63
5.5.3	Heavy Flavour BDT	65
5.6	Systematic uncertainties	69
5.6.1	Uncertainties on Physics Objects	69
5.6.2	Uncertainties on Background Modeling	71
5.7	Statistical method	75
5.7.1	Histogram Treatment	76
5.8	Results	78
6	Conclusion	82

Abstract

This dissertation considers the search for a charged Higgs boson (H^\pm) in proton-proton collisions with centre-of-mass energies of 7 TeV and 8 TeV, using data collected by the ATLAS experiment at the Large Hadron Collider at CERN. The discovery of such a charged Higgs boson would be a clear indication for physics beyond the Standard Model. The first data collected during the LHC Run-I is analysed, searching for a heavy charged Higgs bosons (above the top quark mass). This study covers the $gb \rightarrow tH^\pm \rightarrow ttb$ where one top-quark decays leptonically and the other decays hadronically.

A significant background originating from $t\bar{t}$ processes, in addition to others, may conceal the charged Higgs decay in the data. Methods using boosted decision trees to constrain such backgrounds and provide signal to background discrimination are presented.

Upper limits on the production cross section times branching ratio of H^\pm are derived for the mass range of $200 \text{ GeV} \leq m_{H^\pm} \leq 600 \text{ GeV}$ for six MSSM benchmark scenarios.

Acknowledgements

First and foremost I would like to express my deepest gratitude to my supervisor Prof. Erez Etzion, for giving me the opportunity to be his student. During my last year as an undergraduate student, Erez did not hesitate to send me to FermiLab. Upon thanking him, he only replied in wishing it will convince me to pursue a scientific path. In his elegant way, he knew always how to steer me in the right direction. I could not have imagined having a better advisor and mentor for my M.Sc. study.

I want to give a special thank you to Dr. Yan Benhammou and Meny Ben Moshe. Yan and Meny took me in as an undergraduate student. They taught me detector physics, hard work and so much more. Thanks to them, the lab felt like a second home.

Finally, I would like to thank the most important person in my life, my wife Yamit, who knew when to hoist the sails for new adventures, but also when to drop anchor and keep a tight watch for me studying. Thank you for pushing me higher and higher every single day.

Chapter 1

Introduction

Nowadays, we know that the Standard Model (SM) is not a complete description of particle physics, it is expected to be, at worst, incomplete rather than wrong, a subset of the true theory of particle physics.

Physicists are searching extensively for a clue of new phenomena that could indicate physics beyond the Standard Model (BSM). Rich and complex theories has, and still are, being developed, all in order to explain various potential deviations which are not fully consistent with the SM.

The discovery of a new neutral scalar particle at the Large Hadron Collider (LHC) in 2012 [1, 2], with a measured mass of 125 GeV [3] raises the question of whether this new particle is the Higgs boson of the SM, or one physical state of an extended Higgs sector which may contain also an additional charged scalar particle. The observation of such particle would clearly indicate new physics beyond the SM.

This thesis is based on the paper "*Search for charged Higgs bosons in the $H^\pm \rightarrow tb$ decay channel in pp collisions at $\sqrt{s} = 8$ TeV using the ATLAS detector*" [135] written jointly

with the other members of the analysis team. It is organized as follows. In chapter 2, the theoretical background is laid out. Chapter 3 draws an outline of the LHC accelerator at the CERN laboratory, followed by description of the ATLAS detector (chapter 4). Chapter 5 describes the search for charged Higgs via tb channel. Chapter 6 summarizes and concludes the thesis.

Chapter 2

Theoretical background

2.1 The Standard Model of particle physics

2.1.1 Particles of the Standard Model

The Standard Model of elementary particles [5–7], which was developed in the 1960s and 1970s, has stood for years as "the" theory of particle physics, passing numerous stringent tests. The Standard Model is a theory describing the fundamental constituents, the building blocks of matter and their interactions through electromagnetic, strong and weak forces. The matter particles are elementary, meaning that they do not have an inner structure. They are called fermions, have half integer spin, and can be further categorized into leptons and quarks. The force carriers are bosons, particles with an integer spin. A schematic illustration of the particle content of the SM is given in figure 2.1

The fermions are organized in three families or generations. The Large-Electron-Positron (LEP) experiments at CERN, showed that there are no more than three families



Figure 2.1: Standard Model particle content. Each square stands for an elementary particle and states its characteristic - charge, color charge, mass and spin. The twelve fermions are divided into six quarks and six leptons sorted in three generations with increasing mass from left to right. The force mediator bosons shares a rectangle with the fermions affected by the force they carry [4].

with light neutrinos in the SM [8]. Each family consists of two quarks and two leptons. The quarks can be categorized into one up-type quark with an electric charge of $+\frac{2}{3}e$ and one down-type quark with an electric charge of $-\frac{1}{3}e$. The leptons consists of an electron like lepton and a neutrino. The massive leptons (electron, muon and tau) have an electric charge of $-e$. Neutrinos are electrically neutral and much lighter than the charged leptons. All particles with an electric charge interact electromagnetically, while the neutrino can only interact via the weak force.

Quarks, unlike leptons, also carry a color charge, the quanta of the strong interaction. Quarks come in three colors, ‘red’, ‘green’ and ‘blue’. Additionally, they only exist in a confined state for which the sum of the color charges is white. A Baryon is a three quarks bound state. A proton for example is a baryon consists of three

quarks, two up and one down. A Meson is a two quarks bound state which must have a quark and anti-quark pair. Just recently, [9] a bound state of five quarks (not necessarily all five in the same confinement volume), a penta-quark like structure, was observed at the LHCb experiment at CERN as predicted in [10].

In the SM the forces are being carried out by the gauge bosons. The photon, γ , is the carrier of the electromagnetic force, the W and Z bosons are the carriers of the weak force and the gluons, g , for the strong force.

Up until 2012, almost all of the SM particles have been observed and studied. All but one missing piece, the Higgs boson. It was discovered in 2012 by the ATLAS and CMS experiments at CERN, Geneva [1, 2]. Unlike the rest of the gauge bosons, the Higgs has a different role in the Standard Model as explained further in the following chapters.

In order to claim a discovery, an experiment needs to demonstrate a deviation with 5σ significance level. This will establish that a new particle was discovered with 99.9999% probability and $\leq 0.0001\%$ probability for just a background fluctuation. For the collaborations to get enough sensitivity to claim a discovery, they combined several channels ($H \rightarrow \gamma\gamma, H \rightarrow ZZ, H \rightarrow WW, H \rightarrow \tau\tau, H \rightarrow bb$). Figure 2.2 presents the distribution of the four-lepton invariant mass m_{4l} measured by ATLAS and the invariant mass of di-photon candidates measured by CMS, as a selection of channels in which the Higgs boson with a mass of around 125 GeV was discovered. In July of 2012, both ATLAS and CMS presented results confirming the existence of the Higgs boson. Thereafter, in October of 2013, Peter Higgs and Francois Englert have been awarded the Nobel prize for physics.

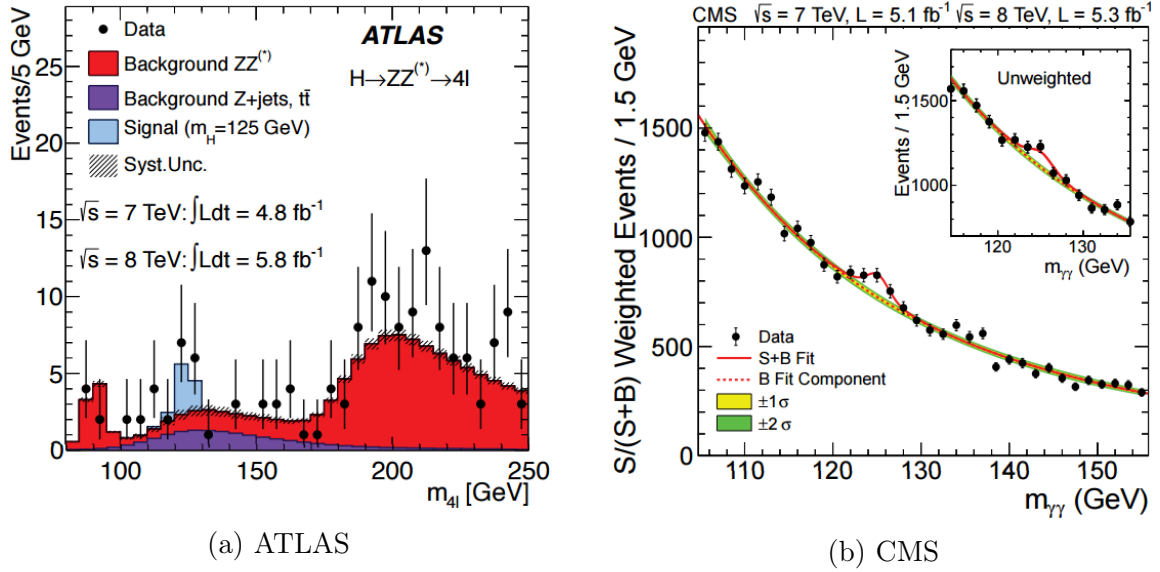


Figure 2.2: Four-lepton invariant mass, m_{4l} , for the selected candidates, measured in ATLAS (left) and the invariant mass distribution of di-photon candidates in CMS (right) as presented in the Higgs discovery papers [1, 2].

2.1.2 Gauge theory of weak interactions

The principle of gauge invariance is perhaps one the most significant of the concepts used in modern particle theories, as it provides an explanation for the origin of the fundamental forces themselves. The basic method of gauge theory is to ensure that the Lagrangian describing the interaction of particle wave-functions remains under certain symmetry transformations which reflect the conservation laws observed in nature [19, 136].

The global phase symmetry $\psi(\mathbf{x}, t) \rightarrow e^{-i\lambda}\psi(\mathbf{x}, t)$, where λ is a constant, is a relatively simple symmetry and does not place a very strong constraint on the form of the Lagrangian. It becomes more interesting if we demand that the theory would be invariant

under *local* phase transformation:

$$\psi(\mathbf{x}, t) \rightarrow e^{-\lambda(\mathbf{x}, t)} \psi(\mathbf{x}, t) \quad (2.1)$$

$$\mathbf{G}(\mathbf{x}, t) \mathcal{L}(\psi) \rightarrow \mathcal{L}^*(\psi^*) \quad (2.2)$$

For instance, a local gauge transformation corresponds to choosing a convention for defining the phase of an electron wavefunction. This electron wavefunction is different at various space-time points. That is, the convention can be decided independently at every point in space and at every moment in time. Yet, due to space-time dependence, the Lagrangian representing the electron wavefunction is changed by local gauge transformation and the theory is not invariant anymore. However, by introducing another field, which compensates for the local change in the electron wavefunction, we can obtain a Lagrangian that indeed exhibits such symmetry.

This requirement must have infinite range, since there is no limit to the distances over which the phase conventions must be reconciled. Hence, the quantum of the new field must be massless. For the electromagnetic field, the one who is meeting this requirement is of course, the photon.

In formulating a sensible theory of the weak interactions, one has to incorporate the basic laws of leptonic physics. It is natural, therefore, to group the leptons wavefunction into doublets of the same lepton-type:

$$l_e = \begin{pmatrix} \nu_e \\ e^- \end{pmatrix} \quad l_\mu = \begin{pmatrix} \nu_\mu \\ \mu^- \end{pmatrix} \quad l_\tau = \begin{pmatrix} \nu_\tau \\ \tau^- \end{pmatrix}$$

Thus, one can define a 'weak isospin' with analogous to the isospin of nucleons. While doing so, to require that the weak interaction be invariant under rotations in this weak isospin space. Denoted by $SU(2)^W$, the group of weak isospin rotations should transform the Lagrangian invariantly:

$$\mathbf{G}^{SU(2)^W} \mathcal{L}(l_e, l_\mu, l_\tau) \rightarrow \mathcal{L}(l_e^*, l_\mu^*, l_\tau^*).$$

Enforcing such symmetry requires the introduction of massless gauge particles, W , to guarantee the invariance of the Lagrangian:

$$\mathbf{G}^{SU(2)^W} \mathcal{L}(l_e, l_\mu, l_\tau, W) \rightarrow \mathcal{L}(l_e^*, l_\mu^*, l_\tau^*, W^*).$$

Experiments showed [11–14] that the gauge bosons, besides the photon and gluon, have masses. Introducing explicit mass terms in the SM generates problems with gauge invariance and renormalization, making it impossible to predict observables with good accuracy. Hence, there has to be a different mechanism for the weak gauge bosons mass in the SM. This can be achieved by introducing spontaneous symmetry breaking [15, 16].

2.1.3 Spontaneous symmetry breaking and the Higgs mechanism

Asymmetric solution to a symmetric theory exists in many branches of physics and real life. A simple mechanical example is the behavior of a ball inside the bottom of a wine bottle. This kind of potential is referred to as a "Mexican-Hat" potential (see figure 2.3). Obviously, the symmetric state is when the ball is at the center of hump, yet, it is not the ground state of the system, a state with minimum energy. Any small perturbation will

send the ball tumbling down into the trough, where the system possess least energy, but is also rotationally asymmetric. When the symmetry of a physical system is broken this way by an asymmetric ground state, we say the system exhibits 'spontaneous symmetry breaking'.

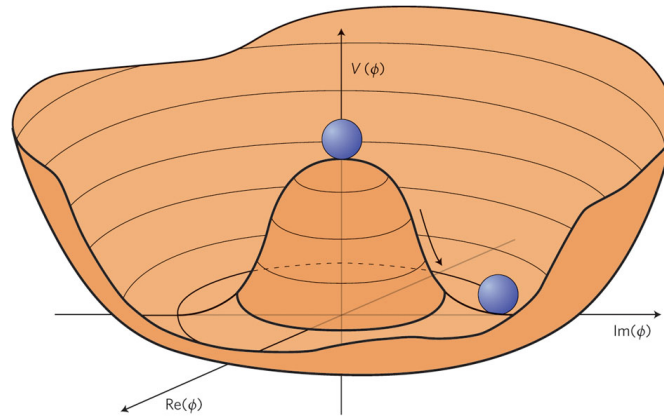


Figure 2.3: In other words, the marble simply wants to roll down to the valley, in a random direction. It has to randomly choose the direction because they're the same a priori, and this choice is what "spontaneously breaks the symmetry".

One could consider a hypothetical spinless particle consisting of two components :

$$\Phi = \begin{pmatrix} \phi_1(\mathbf{x}, t) \\ \phi_2(\mathbf{x}, t) \end{pmatrix} \quad \phi_1 = \Im(\phi), \quad \phi_2 = \Re(\phi) \quad (2.3)$$

Suppose we chose a Mexican-Hat shaped potential to describe the interaction energy such as figure 2.3. For this kind of interaction, the energy is not minimum for zero values of the fields, but around the circle defined by $\phi_1^2 + \phi_2^2 = R^2$. Of course our Lagrangian is still describing the same physics since it is merely a redefinition. However, an interesting features now arouses. First, the vacuum is not invariant under the original group \mathbf{G} of rotations. Second, the Lagrangian now describes ϕ_2' as a massive particle

(mass proportional to R), and ϕ'_1 as a massless particle. Unfortunately, the presence of the massless spin-0 particle turns out to be a general consequence of this type of mechanism. Whenever a global symmetry is spontaneously broken, a massless spin-0 particle results. This particle is called a 'Goldstone boson' [17]. In our current understanding, no such massless, spinless particle had been observed.

The problem is solved by *local* gauge transformation. Demanding that, will result in introducing a new gauge particle which will be denote by W . Rewriting the Lagrangian in the same way we did before will result in something remarkable. The redefined ϕ'_2 particle acquires, as before, a mass proportional to R , but the massless Goldstone boson ϕ'_1 disappears, one may say, got "eaten" by it's massive partner. Moreover, the formally massless gauge particle W now acquires a mass, again, proportional to R .

Deriving the Higgs mechanism follows the same principles of Quantum Field Theory (QFT) [18]. As defined in equation 2.3, a complex Higgs $SU(2)$ doublet is included in the SM, with a $SU(2) \times U(1)$ invariant Lagrangian [19]:

$$\mathcal{L}(\mathbf{x}, t) = [D^\mu \Phi(\mathbf{x}, t)]^\dagger [D_\mu \Phi(\mathbf{x}, t)] - V(\Phi(\mathbf{x}, t)) \quad (2.4)$$

where Φ^\dagger is the Hermitian conjugate of Φ and $V(\Phi)$ is the Higgs potential of the form:

$$V(\Phi(\mathbf{x}, t)) = \mu^2 (\Phi^\dagger(\mathbf{x}, t) \Phi(\mathbf{x}, t)) + \lambda (\Phi^\dagger(\mathbf{x}, t) \Phi(\mathbf{x}, t))^2 \quad (2.5)$$

With boundary conditions $\mu^2 < 0$ and $\lambda > 0$, the potential takes the form of a Mexican-hat. D_μ is the gauge covariant derivative, containing the interaction terms which lead to the gauge bosons.

The Higgs potential has a continuum of minima. The electroweak symmetry can be broken by choosing one minimum using the freedom of a global SU(2) rotation. A convenient choice for such a vacuum state is:

$$\Phi_0 = \begin{pmatrix} \phi_1^0(\mathbf{x}, t) \\ \phi_2^0(\mathbf{x}, t) \end{pmatrix} = \frac{1}{\sqrt{2}} \begin{pmatrix} 0 \\ \nu \end{pmatrix}, \quad \nu = \sqrt{-\frac{\mu^2}{\lambda}} \quad (2.6)$$

Expanding around the vacuum state gives:

$$\Phi_0 = \frac{1}{\sqrt{2}} \begin{pmatrix} \eta_1(\mathbf{x}, t) + i\eta_2(\mathbf{x}, t) \\ \nu + \sigma(\mathbf{x}, t) + i\eta_3(\mathbf{x}, t) \end{pmatrix} \quad (2.7)$$

where $\eta_i(\mathbf{x}, t)$ and $\sigma(\mathbf{x}, t)$ are scalar fields.

Using this equation in the Lagrangian yields mass terms, by spontaneous symmetry breaking, for the gauge bosons. After diagonalising, the W and Z bosons acquire masses, while the photon γ remains massless. The surviving field σ , with a vacuum expectation value of $\nu = \sqrt{\frac{\mu^2}{\lambda}} = 246 \text{ GeV}$ [4], the average expected value in the vacuum, gives rise to a massive, electrically neutral, spin-0 particle, called the Higgs boson.

It should be noted that the Higgs field can also generate masses for the fermions via Yukawa couplings, this is important because it turns out that chiral gauge invariance forbids explicit mass terms for the fermions as well. Generating fermion masses can be done using the scalar field Φ , with hypercharge $Y = 1$, and the isodoublet $\tilde{\Phi} = i\tau\Phi^*$ with a hypercharge $Y = -1$. τ_2 is the second Pauli matrix. For any fermion generation, the

$SU(2)_L \times U(1)_Y$ invariant Yukawa Lagrangian can be introduced [32]:

$$\mathcal{L} = -\lambda \bar{L} \Phi e_R - \lambda_d \bar{Q} \Phi d_R - \lambda_u \bar{Q} \Phi u_R + h.c \quad (2.8)$$

where \bar{L} and \bar{Q} are the isodoublets of the left-handed fermions for leptons and quarks, respectively and e_R, u_R and d_R are the isosinglets of the righthanded fermions for leptons, up-type quarks and down-type quarks. After gauge transformation the Lagrangian can be written in the form:

$$\mathcal{L} = -\frac{1}{\sqrt{2}} \lambda_f (\nu + \sigma) \bar{f}_L f_R + h.c \quad (2.9)$$

The constant term in front of the fermion isosinglets $\bar{f}_L f_R$ is the mass of the fermion:

$$m_e = \frac{\lambda_e \nu}{\sqrt{2}}, \quad m_u = \frac{\lambda_u \nu}{\sqrt{2}}, \quad m_d = \frac{\lambda_d \nu}{\sqrt{2}}, \quad (2.10)$$

2.2 Beyond the Standard Model (BSM) physics

The Standard Model is one of the great successes of 20th century physics. But even without including gravity, we have good experimental and theoretical reasons to believe that the SM is not the whole story. A deeper conceptual structure may be lurking behind it. The Standard Model signals its own incompleteness in several ways. In the following section a few general examples are laid out.

2.2.1 Phenomena not explained by the Standard Model

The hierarchy problem: One of the most important problems concerns the mass of the Higgs boson. Like all particles, its intrinsic mass would be subject to quantum corrections. By interacting with short lived virtual particles the Higgs should obtain a self-energy, changing its effective mass. It turns out that these corrections are very large, supposedly proportional to energy scales (such as the *Grand Unification Energy*) where new physics effects could be expected to cancel this divergent behavior. The corrections are also dependent on the masses of the other particles, and of the Higgs boson itself, and the only way in the SM to preserve a low Higgs mass is if all these masses cancel each other. Of these, the Higgs boson mass is the only unknown one. Since the corrections are proportional to a very large energy scale, the Higgs boson mass must be chosen very precisely to cancel with the other masses in order to keep the corrections small. This necessary of the Higgs mass is called the *hierarchy problem* [20]. fine-tuning it, is indeed considered a very undesirable and "unnatural" property of any theory to be overly sensitive to small variations of a parameter like this.

Dark matter and dark energy: Observations of the cosmic microwave background show that the SM can explain around 5% of the energy content in the universe. It is believed that around 27% is dark matter and 68% is dark energy [21]. The existence and properties of dark matter are studied from its gravitational effects on visible matter, radiation and large-scale structures of the universe. Dark Energy is used to explain the acceleration of the expansion of the universe. Many theories say the dark matter particles would be light enough to be produced at the LHC. If they were created at the LHC, they would escape through the detectors unnoticed. However, they would carry away

energy and momentum, so one could infer their existence from the amount of energy and momentum $\hat{A}I\text{missing}\hat{A}$ after a collision.

Neutrino mass: In the SM neutrinos are massless and cannot change flavor. The observed number of electron neutrinos arriving from the sun is much smaller than the number predicted by the Standard Solar Model, this is called the solar neutrino problem. To solve this problem neutrinos need to have mass, in order to oscillate between flavors [22].

Matter anti-matter asymmetry: The universe is mainly made of matter, e.g. particles, not anti-particles. The SM predicts that matter and anti-matter were produced in almost equal amounts in the Big Bang. Charge Parity (CP) Violation in the SM, the effect that matter does not exactly behave in the same way as anti-matter under CP transformation, can account for some but not the full SM matter in our universe. Hence the reason for the matter anti-matter asymmetry must be phenomena not explained by the SM [23].

Quantum gravity: Gravity is not included in the SM. Adding gravity to the SM is not possible as it generates nonphysical effects like particle velocities higher than the speed of light, and further modifications would be needed. The most successful theory (General Relativity) is incompatible with the SM [24]. Gravity acts on a macroscopic scale, therefore the SM predictions are not affected by it.

2.2.2 The charged Higgs boson

New theories have been proposed to replace or extend the SM in order to address these problems. Perhaps most notably, supersymmetric (SUSY) [19] theories effectively double

the amount of predicted particles by introducing new symmetries - for each SM fermion there should be a corresponding boson and vice versa. Since no such particles have been observed, SUSY must - if it exists - be broken so that the supersymmetric partner particles obtain higher masses than the ordinary particles. Still, SUSY is very attractive because it offers elegant solutions to some of the problems described above. Quantum corrections to the Higgs mass from supersymmetric particles would effectively cancel those from ordinary particles, eliminating the hierarchy problem. Several Supersymmetric theories predict the existence of a heavy neutral particle called *neutralino* which could possibly make up the cold dark matter in the universe. SUSY models suggest a way to unify the strong, weak and electromagnetic forces into a single force at high energies [25], in a so-called *Grand Unification Theory*.

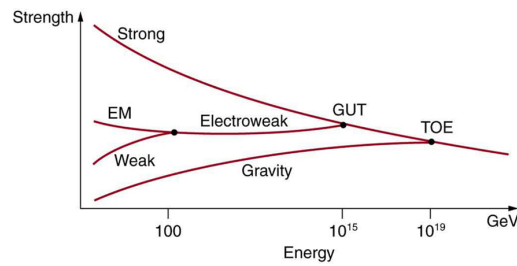


Figure 2.4: The relative strengths of the four basic forces vary with distance and, hence, high energy is needed to probe small distances. At energies available at accelerators, the weak and EM forces become identical, or unified. Unfortunately, the energies at which the strong and electroweak forces become the same are unreachable even in principle at any conceivable accelerator.

As explained in section 2.3, the Standard Model includes a complex doublet Higgs field. Nothing prevents us, however, from adding a second such field to the theory, introducing two more complex $SU(2)$ doublet scalar fields with hypercharge $Y = 1$:

$$\Phi_1 = \begin{pmatrix} \phi_1^+(\mathbf{x}, t) \\ \phi_1^0(\mathbf{x}, t) \end{pmatrix}, \quad \Phi_2 = \begin{pmatrix} \phi_2^+(\mathbf{x}, t) \\ \phi_2^0(\mathbf{x}, t) \end{pmatrix} \quad (2.11)$$

This scenario is called the Two Higgs Doublet Model (2HDM) [19, 28] and arises naturally in e.g. the Minimal Supersymmetric Standard Model (MSSM) [19, 28], the simplest possible extension to the SM that realizes SUSY. The most general 2HDM Higgs potential can be written [26]:

$$V = m_{11}^2(\Phi_1^\dagger \Phi_1) + m_{22}^2(\Phi_2^\dagger \Phi_2) - m_{12}^2(\Phi_1^\dagger \Phi_2 + \Phi_2^\dagger \Phi_1) + \frac{1}{2}\lambda_1(\Phi_1^\dagger \Phi_1)^2 + \frac{1}{2}\lambda_2(\Phi_2^\dagger \Phi_2)^2 + \lambda_3(\Phi_1^\dagger \Phi_1)(\Phi_2^\dagger \Phi_2) + \lambda_4(\Phi_1^\dagger \Phi_2)(\Phi_2^\dagger \Phi_1) + \frac{1}{2}\lambda_5[(\Phi_1^\dagger \Phi_2)^2 + (\Phi_2^\dagger \Phi_1)^2] \quad (2.12)$$

where all the parameters are real. For a region of parameter space, the minimization of this potential gives:

$$\langle \Phi_1 \rangle = \frac{1}{\sqrt{2}} \begin{pmatrix} 0 \\ \nu_1 \end{pmatrix}, \quad \langle \Phi_2 \rangle = \frac{1}{\sqrt{2}} \begin{pmatrix} 0 \\ \nu_2 \end{pmatrix} \quad (2.13)$$

with ν_1, ν_2 as the vacuum expectation values. With two complex scalar SU(2) doublets there are eight fields:

$$\Phi_a = \begin{pmatrix} \phi_a^+ \\ (\nu_a + \rho_a + i\eta_a)\sqrt{2} \end{pmatrix}, \quad a = 1, 2 \quad (2.14)$$

From these eight degrees of freedom, three are getting "eaten" in order to give mass for the W^\pm and Z^0 gauge bosons and the remaining five are the physical scalar Higgs fields. There are two charged scalars (H^\pm), two CP-even neutral scalars H^0 and h^0 , and

one CP-odd pseudoscalar A . With the above minimum, the mass terms for the charged scalars are given by:

$$\mathcal{L}_{\phi^\pm mass} = [m_{12}^2 - (\lambda_4 - \lambda_5)\nu_1\nu_2](\phi_1^-, \phi_2^-) \begin{pmatrix} \frac{\nu_2}{\nu_1} & -1 \\ -1 & \frac{\nu_1}{\nu_2} \end{pmatrix} \begin{pmatrix} \phi_1^+ \\ \phi_2^+ \end{pmatrix} \quad (2.15)$$

There is a zero eigenvalue corresponding to the charged Goldstone boson G^\pm which gets eaten by the W^\pm . The mass-squared of the charged Higgs boson is:

$$m_{H^\pm}^2 = [m_{12}^2/(\nu_1\nu_2) - \lambda_4 - \lambda_5](\nu_1^2 + \nu_2^2) \quad (2.16)$$

At tree level the properties of these particles can be completely determined by two parameters, which can be chosen to be the charged Higgs boson mass m_{H^\pm} and the ratio of the two Higgs doublet vacuum expectation values $\tan(\beta)$:

$$\tan(\beta) \equiv \frac{\nu_2}{\nu_1} \quad (2.17)$$

The angle β is the rotation angle which diagonalizes the mass-squared matrices of the charged scalars and of the pseudoscalars. These two parameters, m_{H^\pm} and $\tan(\beta)$, define a phase-space for searches of such particle.

Chapter 3

The CERN laboratory

The world largest laboratory for particle physics CERN¹ (Conseil Européen pour la Recherche Nucléaire), is located to the north-west of Geneva on the French-Swiss border. It was founded on the 29th of September 1954. Today, CERN has twenty-one member states and several hundred universities worldwide participating in the research conducted there. At the beginning CERN was a laboratory for nuclear research but the energy frontier quickly moved on to higher energies to study more fundamental particles. CERN is the provider of the particle accelerators and other main infrastructure needed to the high energy frontier. The experiments at the accelerators are constructed by international collaborations. Although mostly associated with particle physics, CERN also contributes to achievements in computing science and engineering science. For example, the World Wide Web was invented at CERN.

¹The European Organization for Nuclear Research

3.1 The accelerator infrastructure

CERN is the provider of the acceleration and de-acceleration infrastructure, producing particles at different energies for the experiments. The interplay between the different accelerator stages at CERN is shown in figure 3.1. The various accelerators in the LHC complex are listed and described in the following:

3.1.1 Linear accelerators

For the LHC to accelerate particles, several linear accelerators (LINAC) are stationed within the complex:

- **LINAC-2** [33] accelerates protons after the ionization of hydrogen to an energy of 50 MeV with a pulse length of 1 Hz and a current of 175 mA. Its main purpose is to be a pre-accelerator for the Proton Synchrotron Booster (PSB).
- **LINAC-3** [34] is a second linear accelerator at CERN, for heavy ions instead of protons. After stripping off all electrons, it accelerates ions to an energy of 4.2 MeV/nucleon. Subsequently, the ions are injected into the Low Energy Ion Ring (LEIR).
- **LINAC-4** [35] is a future linear proton accelerator, that will replace Linac-2 in 2017/2018. Its construction was approved in 2007 and it is needed in order to provide enough protons to be able to reach the design luminosity of the LHC. Protons will be accelerated to an energy of 160 MeV.

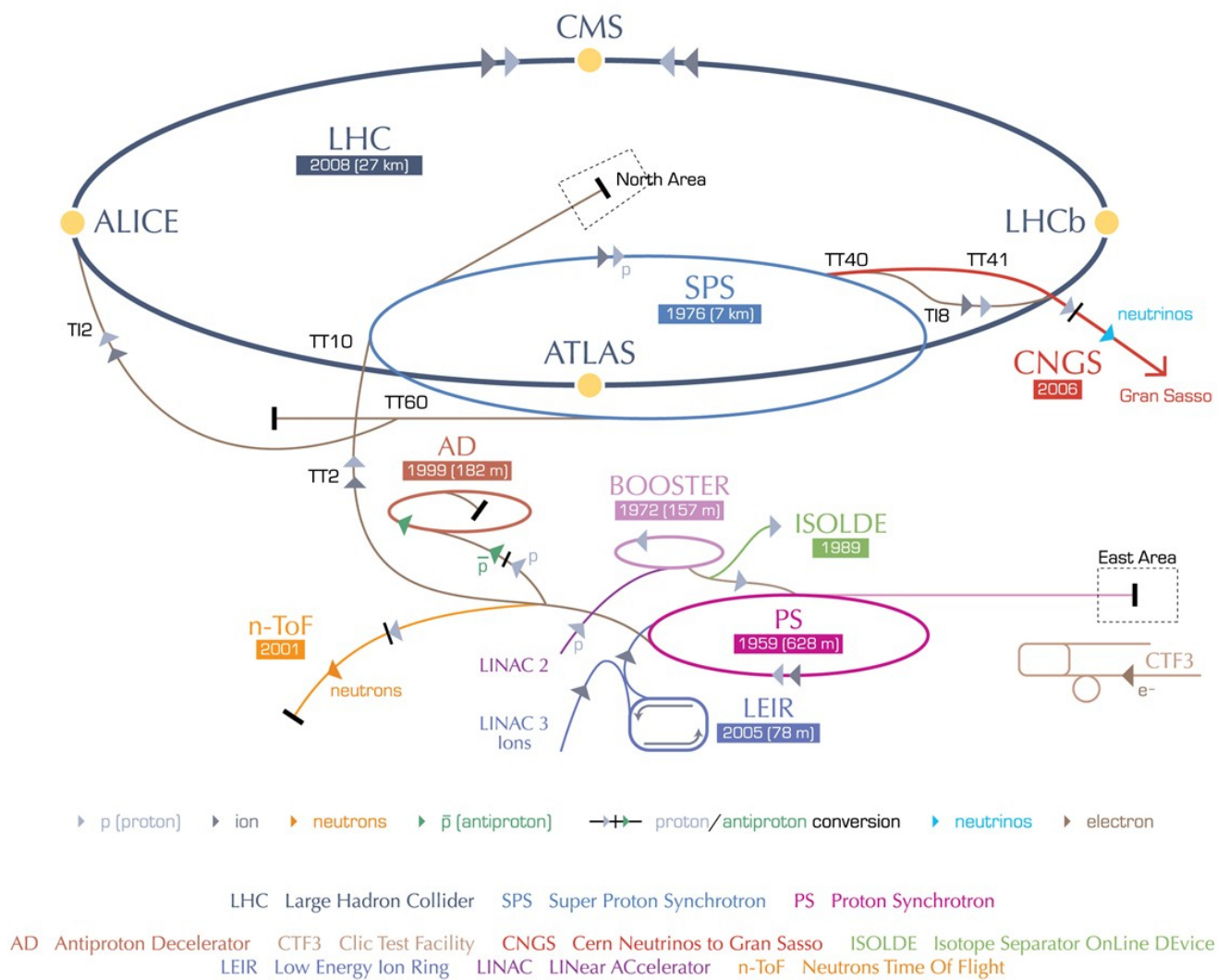


Figure 3.1: CERN accelerator complex [36].

3.1.2 Proton Synchrotron Booster (PSB)

The Proton Synchrotron Booster [37] is one of the pre-accelerators at CERN. It receives the protons from Linac-2 and accelerates them to an energy of 1.4 GeV. The protons are subsequently injected into the Proton Synchrotron or delivered to Isolde [38] to produce radioactive ion beams.

3.1.3 Proton Synchrotron (PS)

The Proton Synchrotron [39] is a key accelerator at CERN. It gets protons from the PSB or ions from the LEIR and accelerates them to higher energies. Protons can reach energies up to 28 GeV and ions up to 72 MeV/nucleon. The Proton Synchrotron acts as a pre-accelerator for the Super Proton Synchrotron. Its protons can also be used for anti-proton production for the Anti-proton Deaccelerator (AD), production of neutrons and beam delivery to the East Area of CERN.

3.1.4 Super Proton Synchrotron (SPS)

The Super Proton Synchrotron is the second largest accelerator at CERN. It is 6.9 km in circumference and can accelerate protons to energies up to 450 GeV. Before the LHC era, it was used as the proton-anti-proton collider for the UA1 and UA2 experiments. Today it acts as a pre-accelerator for the LHC, but it also has delivered protons for the neutrino beam to Gran Sasso (CNGS) and it provides a proton beam for the fixed target experiments in the North Area of CERN. There are plans to further upgrade the SPS to a Super-SPS in order to reach the design luminosity in LHC.

3.2 The Large Hadron Collider (LHC)

The Large Hadron Collider [40] provides the highest collision energy in the world, required for precision studies of the Standard Model and to probe new physics beyond it. The LHC is built in the former Large Electron Positron collider (LEP) tunnel with a circumference of 27 km, which allows operation at a centre-of-mass energy of up to 14 TeV for proton-proton collisions and a luminosity of $10^{34} \text{ cm}^{-2}\text{s}^{-1}$. In addition to proton-proton collisions, the LHC provides heavy ion collisions for studies of quark-gluon plasma. More than 10,000 scientists and engineers from hundreds of universities are using the beams of the LHC for their research. This work is done by four collaborations ALICE, ATLAS, CMS, LHCb, each with an experimental facility at four points along the LHC ring, the locations are shown in figure 3.2

The start-up of the LHC was on the 10th of September 2008, but was stopped after a short time due to a major accident with the magnet system. On the 20th of November 2009, the LHC restarted and successfully collided protons after a few days. The first collisions were at an energy per beam of 450 GeV, the injection energy of the SPS. The beam energy was increased in steps and after the winter shut-down in 2009/2010, the energy per beam reached 3.5 TeV, half of the design energy of the LHC. In 2012 a further increase to 4 TeV per beam was achieved. More than 5 fb^{-1} of integrated luminosity were recorded at a centre-of-mass energy of 7 TeV and more than 21 fb^{-1} of data with a centre-of-mass energy of 8 TeV. At the end of 2012, the LHC was shut down for maintenance and upgrades for two complete years. In march 2015, the LHC started accelerating once more, this time delivering collisions at energy of 13 TeV.

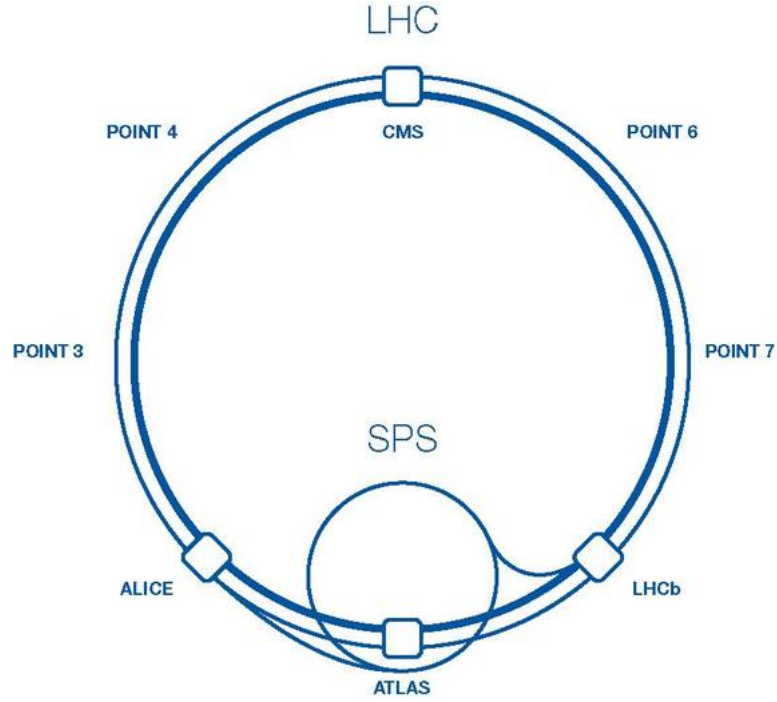


Figure 3.2: Schematic of the LHC ring, with the positions of the experiments [40, 41]

3.3 LHC experiments

ALICE (A Large Ion Collider Experiment) [42] is a heavy ion experiment designed to study the conditions of the universe directly after the Big Bang. Heavy ion runs are used to produce temperatures 100 times higher than inside the sun to produce quark-gluon plasma.

CMS (Compact Muon Solenoid) [43] is in size the second biggest experiment at the LHC. It is a general purpose detector, designed for searching the Higgs boson, for supersymmetry, dark matter and for precision measurements of the Standard Model. The detector is built inside a big 4 T solenoid magnet. CMS was the only detector at the LHC built over ground and installed in 15 slices in the CMS cavern. The detector system has

a length of 21 m, a width of 15 m and a height of 15 m. It weighs 12500 t.

LHCb (Large Hadron Collider beauty) [44] is a detector system designed to study the B-mesons in detail. The focus is the study of the matter-antimatter symmetry and rare decays of B-mesons, which are sensitive to new physics beyond the Standard Model. It is the smallest detector at the LHC build as a single arm spectrometer detecting particles propagating in the forward direction. The experiment does not use the full luminosity of the LHC to avoid pile-up² events.

ATLAS (A Toroidal LHC ApparatuS) [27] is the largest detector at the LHC. It is like CMS, a general purpose detector with the same physics goals. More details about the ATLAS detector system, which was used to collect the data used in this thesis, are described in the next chapter.

²pile-up: In high-luminosity colliders, there is a non-negligible probability that one single bunch crossing may produce several separate events, so-called pile-up events. [45]

Chapter 4

The ATLAS detector system

This chapter provides a basic introduction to the ATLAS detector. Focus is given to the detectors used in the work presented in this thesis. More information about the design, construction and operation of the ATLAS detector can be found in References [27, 46–48].

4.1 Overview

The ATLAS detector is centered on one of the LHC collision points. Shown in figure 4.1, ATLAS is over 24 meters high and almost 45 meters long. It weighs approximately 7000 tons. ATLAS is built around the LHC beam pipe, 100 meters underground. The beam pipe is centred on the cylindrical axis of symmetry of the detector. ATLAS offers a rich set of opportunities for new physics and a possibility to study strongly interacting matter at high energy densities.

Particles produced in the collisions emerge from the center of the detector in all directions. ATLAS has been designed to record the paths and energies of the particles

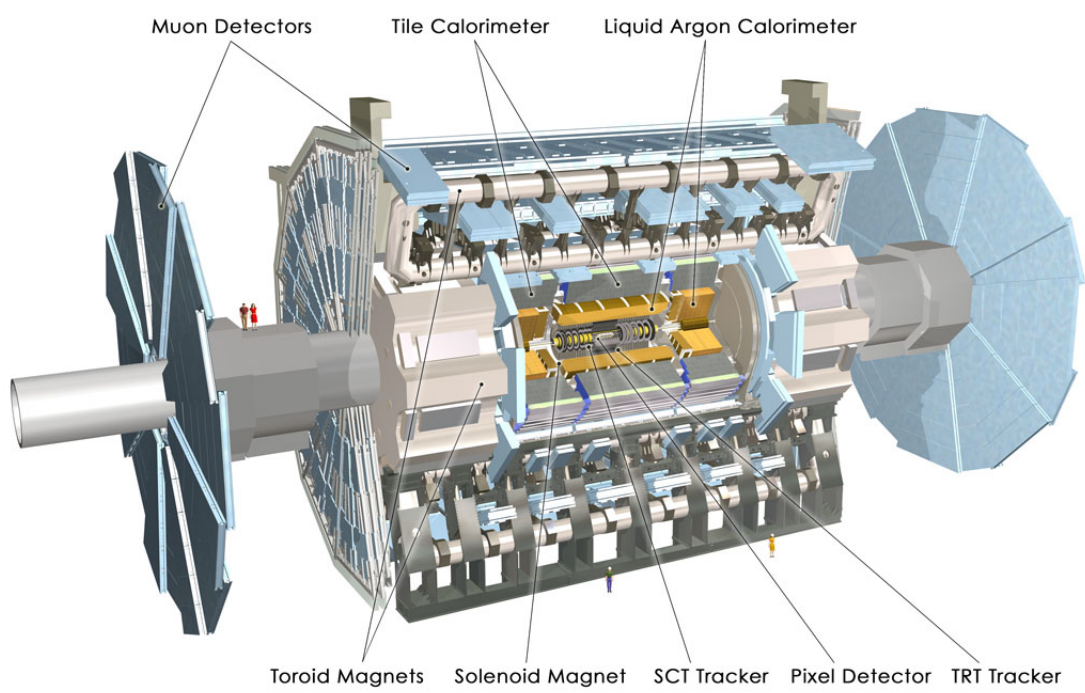


Figure 4.1: Cut-away view of the ATLAS detector.

emerging from the collisions. ATLAS is composed of a series of concentric sub-systems, each sensitive to different types of particles produced in the collisions. The Inner Detector (ID) [49, 50] is closest to the interaction point and measures the trajectories of charged particles. The ID is composed of the Pixel Detector [51, 52], the Semiconductor Tracker (SCT) [53–55], and the Transition Radiation Tracker (TRT) [56–58]. The ID operates in a 2 Tesla magnetic field provided by the solenoid magnet [59]. Surrounding the ID is the calorimeter system [60]. The calorimeter system is composed of the liquid argon electromagnetic calorimeters [61], the tile calorimeters [62], the liquid argon hadronic end-cap calorimeters, and the forward calorimeters. These are each indicated in figure 4.1. The calorimeters are designed to measure the energy of electrons, photons, and hadrons.

The Muon Spectrometer (MS) [63] surrounds the calorimeters. All particles except muons and neutrinos are stopped by the calorimeter system. The MS is designed to measure the trajectories of muons leaving the calorimeter. The MS is composed of muon chambers operating in a magnetic field, provided by the toroid magnetics [64, 65].

4.2 Conventions

A common coordinate system is used throughout ATLAS. The interaction point is defined as the origin of the coordinate system. The z -axis runs along the beam line. The $x - y$ plane is perpendicular to the beam line and is referred to as the transverse plane. Particle momenta measured in the transverse plane is referred to as the transverse momenta, p_T . The positive x -axis points from the interaction point to the center of the LHC ring; the positive y -axis points upward to the surface of the earth. The detector half at positive z -values is referred to as the “A-side”, the other half the “C-side”. The

transverse plane is often described in terms of $r - \phi$ coordinates. The azimuthal angle ϕ is measured from the x -axis, around the beam. The radial dimension, r , measures the distance from the beam line. The polar angle θ is defined as the angle from the positive z -axis. The polar angle is often reported in terms of pseudorapidity, defined as $\eta = -\ln \tan(\theta/2)$. The distance ΔR is defined in $\eta - \phi$ space as $\Delta R = \sqrt{\Delta\eta^2 + \Delta\phi^2}$. Transverse quantities like transverse momentum p_T , transverse energy E_T and missing transverse energy E_T^{miss} are defined in the $x - y$ plane. The 4-momentum vector $\mathbf{P} = (E, p_x, p_y, p_z)$ can be expressed in terms of E, η, ϕ and p_T by $\mathbf{P} = [E, p_T \cos(\phi), p_T \sin(\phi), p_T \sinh(\eta)]$ for massless particles

4.3 Inner detector

The ID measures the position of charged particles as they traverse the detector. In order to cope with the high particle densities produced by the LHC, the ID has been designed to make high-precision measurements with fine detector granularity. The ID operates in a 2 Tesla magnetic field provided by the solenoid magnet. This allows the ID to serve as a spectrometer in which the curved trajectories of charged particles can be reconstructed. Charged particles with transverse momentum above 500 MeV are reconstructed in the ID. Below 500 MeV , charged particles do not cross the full ID.

The ID consists of three sub-detectors built using two technologies: silicon sensors and straw drift tubes. When charged particles cross the silicon sensors, they generate electron-hole pairs that can be collected with an applied electric field. This charge is recorded locally in the sensor, identifying the position of the particle. A similar process occurs in the straw drift tubes. Charged particles traversing the drift tubes ionize gas

contained within the straw. The liberated electrons are drifted, with an applied electron field, to the wire at the center of the straw, where they are recorded. Unlike the silicon sensors, in drift tubes, the primary ionization is multiplied before detection.

The ID is composed of modular collections of sensors. It is built around the beam pipe with a cylindrical geometry. The ID consists of central barrel layers, centred on the interaction point, and end-cap wheels or disks at either end of the barrel. Figure 4.2 shows a cutaway of the ID barrel, and figure 4.3 shows a cutaway of one of the ID end-caps.

The Pixel detector is the closest sub-detector to the interaction point and provides the finest granularity. Comprised of over 80 million channels, the Pixel detector provides on average three measurements per charged particle and has a position resolution of $10\ \mu m$ in the $r - \phi$ plane and $115\ \mu m$ along z . The Pixel detector provides uniform coverage in ϕ , up to $|\eta| = 2.5$.

The SCT surrounds the Pixel detectors. Each SCT layer is composed of a double layer of silicon strips, whose axes are tilted by 40 mrad with respect to one another. The pair of measurements at each SCT layer locates charged particles in $r - \phi$, with an accuracy of $17\ \mu m$, and along z , with an accuracy of $580\ \mu m$. The SCT provides between four and nine measurements per particle, with coverage up to $|\eta| = 2.5$. In total, the SCT is comprised of about 6 million channels.

The TRT is the largest of the sub-detectors in the ID. The TRT is composed of about 300,000 straw drift tubes that provide position measurements with an accuracy of $130\ \mu m$ in ϕ . A large number of hits, around 35 per particle, is provided, with coverage up to $|\eta| = 2.0$.

In addition to being a tracking detector, the TRT also provides particle identification

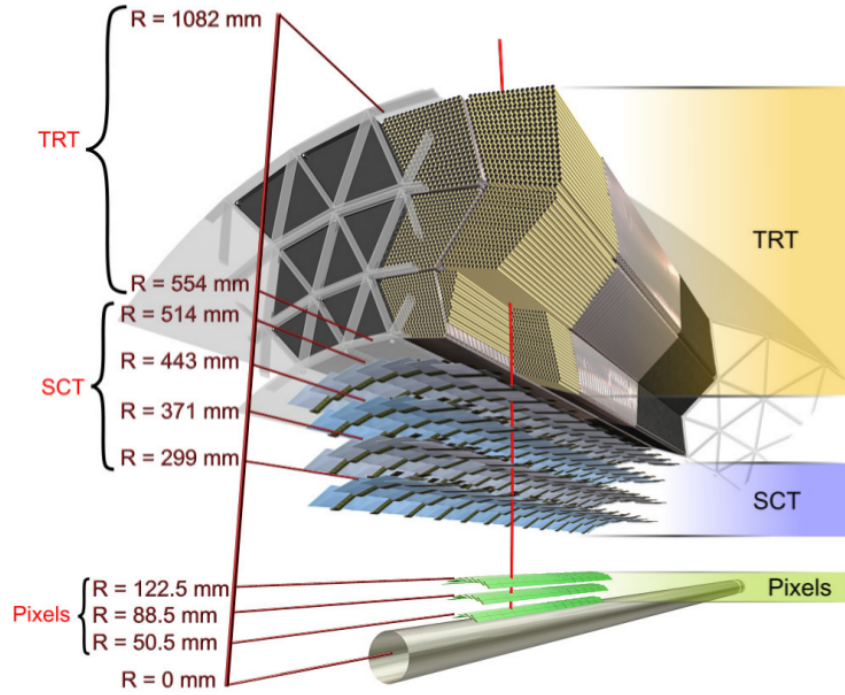


Figure 4.2: Drawing showing the detector elements crossed by a charged particle with 10 GeV p_T in the barrel of the Inner Detector. The particle emerges from the interaction point and traverses the beam-pipe, three pixel layers, four double layers of SCT sensors, and around 35 TRT straws

through the detection of transition radiation. Charged particles emit transition radiation (TR) photons when traversing the TRT. The probability of emitting a TR photon is a function of the Lorentz factor- γ . At a fixed momentum, electrons will emit more transition radiation photons than charged hadrons. The number of TR photons detected in the TRT provides separation between electrons and charged hadrons.

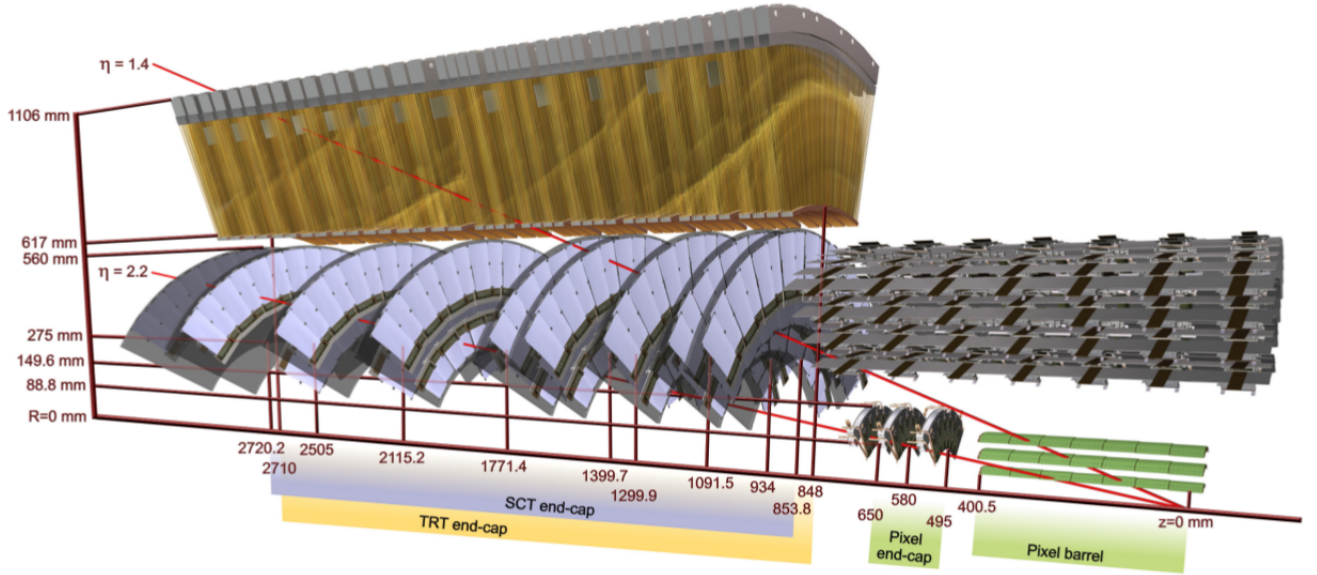


Figure 4.3: Drawing showing the detector elements crossed by two charged particles of 10 GeV p_T in the end-cap of the Inner Detector. A particle at $|\eta| = 1.4$ traverses the beam-pipe, three pixel layers, four SCT disks with double layers of sensors, and approximately 40 straws in the TRT end-cap. A particle at $|\eta| = 2.2$ traverses the beam-pipe, only the first layer of the pixel detector, two end-cap pixel disks and the last four disks of the SCT end-cap. The coverage of the end-cap TRT does not extend beyond $|\eta| = 2$.

4.4 Calorimeters

The calorimeter system measures the energy of hadrons, electrons and photons¹. It provides coverage up to $|\eta| = 4.9$, using several different technologies. An overview of the calorimeter system is shown in figure 4.4. The calorimeter system provides containment for both electromagnetic and hadronic showers, stopping particles before they reach the muon system

The ATLAS calorimeters are a type known as "sampling" calorimeters. Incident parti-

¹Muons leave small fraction of energy in the calorimeters as well. But, their energy cannot be said to be measured by the calorimeters, it is the combined measurement alongside the spectrometer's data that provides the full muon energy.

cles produce showers of energy in the calorimeter. Only a fraction of the energy produced by the particle is measured by active detector sensors. The energy of the full shower can be inferred from the observed energy.

The energies of electrons and photons are measured by the liquid-argon (LAr) electromagnetic (EM) barrel and end-cap calorimeters. The EM calorimeter is a lead-LAr detector with a specialized geometry that provides complete and uniform ϕ coverage and fast readout. These detectors provide high granularity measurements, critical for particle identification in the range $|\eta| < 2.5$. The EM calorimeter is segmented into three radial sections with different $\eta - \phi$ granularities. Figure 4.5 shows a cutaway of the different layers in the EM barrel calorimeter. The first layer, referred to as the “strips”, provides very fine segmentation in η . The strips can separate between showers initiated by electrons or photons and showers initiated by neutral pions. The second sampling provides most of the energy measurement and has fine segmentation in both η and ϕ . The third sampling is coarser and adds additional depth to the calorimeter. The EM calorimeters cover the pseudorapidity range $|\eta| < 3.2$.

The Tile calorimeters and the LAr hadronic end-cap calorimeter are designed to measure the energy of hadrons. The range $|\eta| < 1.7$ is covered by the Tile calorimeter. The scintillator-tile calorimeter is separated into a barrel and two extended barrel cylinders. In the end-caps, $1.5 < |\eta| < 3.2$, LAr technology is used for the hadronic calorimeters. The LAr forward calorimeters provide both electromagnetic and hadronic energy measurements and extend the pseudorapidity coverage to $|\eta| = 4.9$.

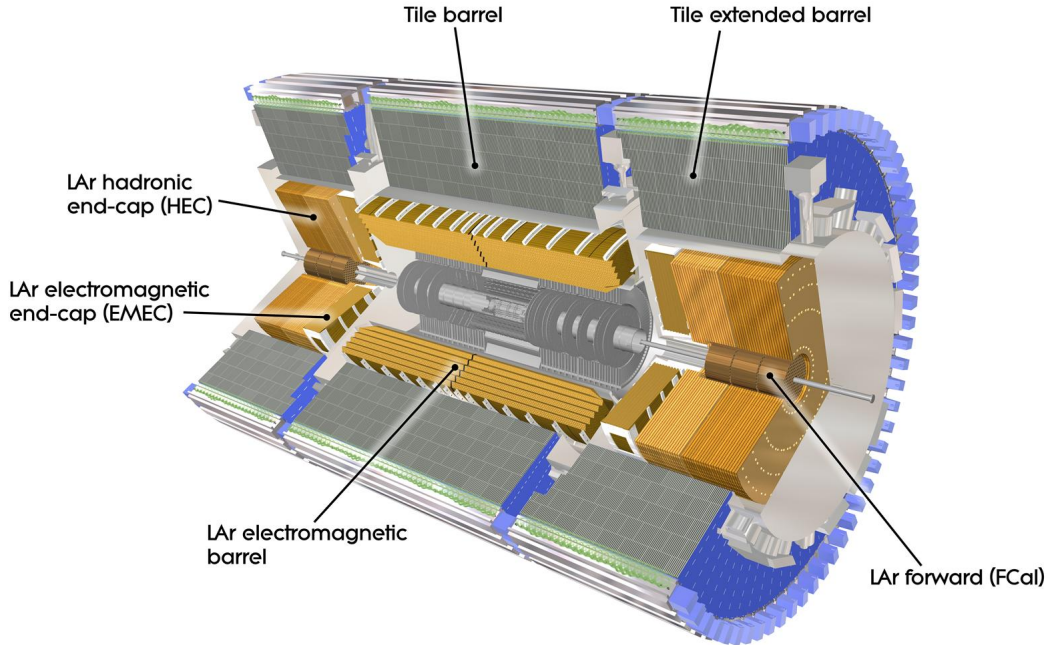


Figure 4.4: Cut-away view of the ATLAS calorimeter system.

4.5 Muon spectrometer

In the ATLAS muon system, the momentum of muons is determined in a large superconducting air-core toroid magnet system. It contains detector technologies for fast triggers and high precision tracking with $60\ \mu\text{m}$ intrinsic resolution. Emphasis is put on reliable, high resolution, stand alone performance over a p_T range from 5 GeV to 1000 GeV. Good momentum resolution is needed, above large backgrounds, for the detection of decays involving muons. The resolution can be further improved by combining the stand alone results of the muon spectrometer with these of the inner detector. An example are light charged Higgs boson searches, where the decay product has one or two leptons. A

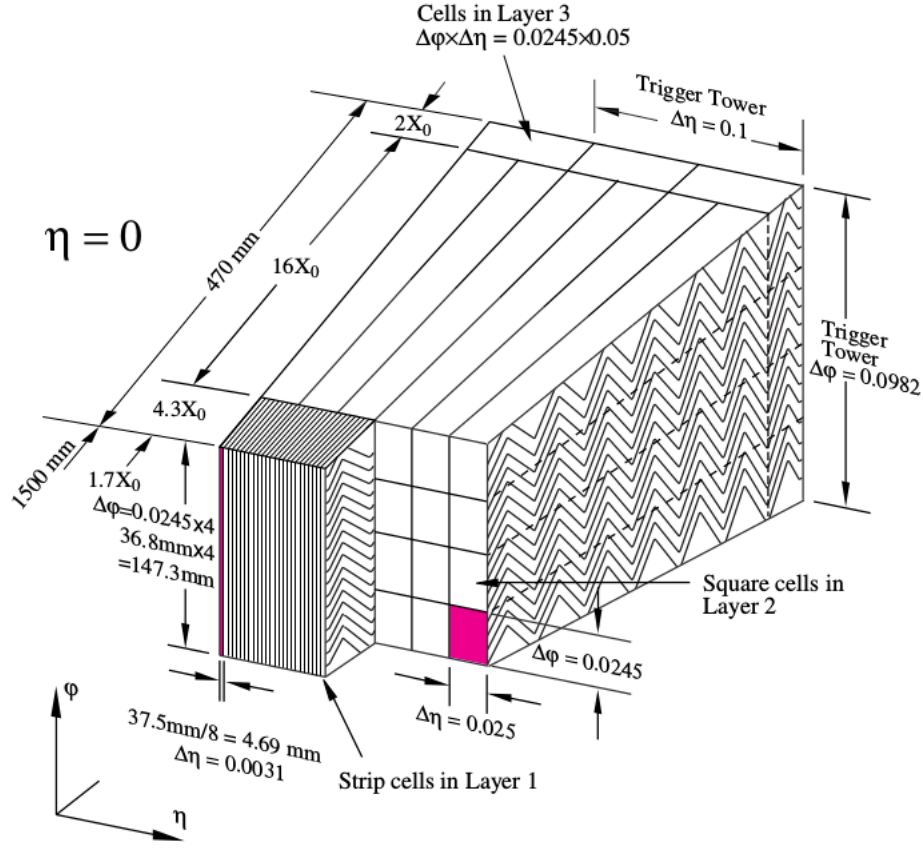


Figure 4.5: Sketch of section of the LAr EM barrel where the different layers are clearly visible. The granularity in η and ϕ of the cells of each of the three layers is shown.

schematic view of the muon system is shown in figure 4.6.

A large central toroid magnet bends the muons in the region $|\eta| < 1.4$. In the high- η regions ($1.6 < |\eta| < 2.7$), two smaller toroidal superconducting magnets are inserted. Each of the three magnets is made from eight coils which are placed symmetrically around the beam axis. A magnetic bending power of 1.4 to 5.5 Tm is provided by the barrel toroid in the range $|\eta| < 1.4$. In the end cap region, a bending power of 1 to 7.5 Tm is provided by the end-cap magnets. The region $1.4 < |\eta| < 1.6$ is called the transition region, where the magnetic fields overlap. Muon chambers arranged in three cylindrical layers around

the beam pipe are used in the barrel region to measure muon tracks. The transition and end-cap regions are covered by three layers of muon chambers arranged along ϕ , meaning the center point of the tubes are oriented tangential to the circle around the beam axis.

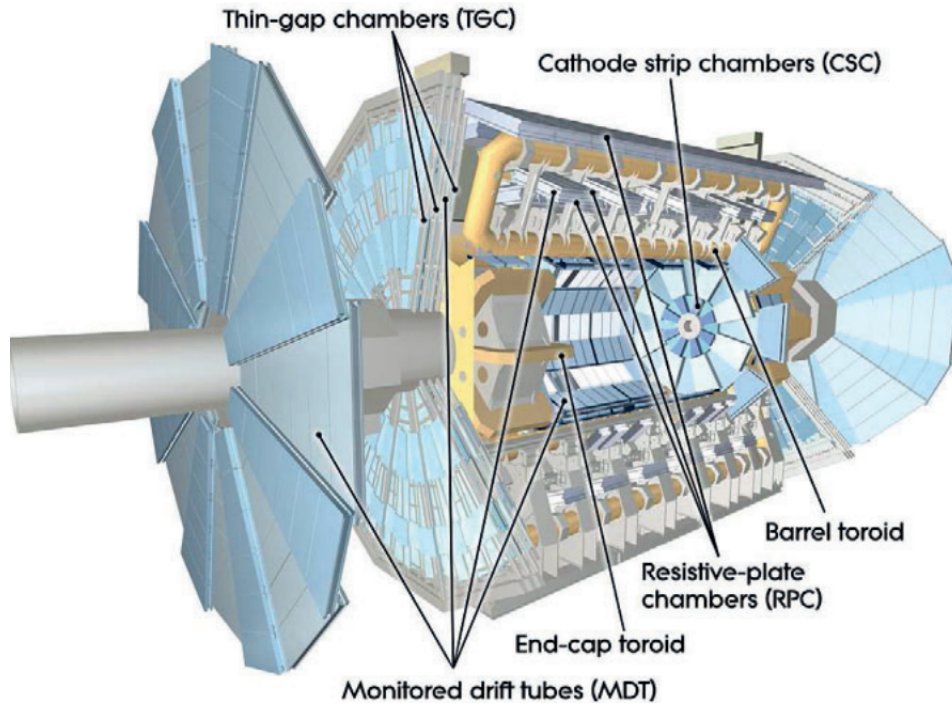


Figure 4.6: Overview of the ATLAS muon system

The region with $|\eta| < 2.7$ is covered by **Monitored Drift Tubes** (MDT). In the high- η region the rates and background conditions are expected to be up to 30 kHz per tube at full LHC luminosity. The MDTs, which are filled with Ar/CO_2 gas, have a diameter of 29.97 mm providing an average resolution of 60-80 μm . The maximal count rate of the MDT is $150 \text{ Hz}/\text{cm}^2$.

Cathode Strip Chambers (CSC) are used in the region $2 < |\eta| < 2.7$ where the particle flux and the density of tracks are highest. The CSC can handle counting rates up

to 1000 Hz/cm^2 . The CSC system is made of two disks of eight chambers, which enable the measurement of η and ϕ coordinates. The CSC is filled with an Ar/CO_2 mixture, the resolution reached is $60\text{ }\mu\text{m}$.

Trigger chambers provide fast information to the Level 1 trigger logic about muon transverse momentum and bunch-crossing identification. The trigger chambers measure the ϕ coordinate to give a full space trajectory in combination with the η coordinate of the MDTs. The region $|\eta| < 2.4$ is covered using two different types of technologies. In the barrel region $|\eta| < 1.05$, **Resistive Plate Chambers** (RPC) are used and, in the region $1.05 < |\eta| < 2.4$, **Thin Gap Chambers** (TGC) are used.

4.6 Trigger system

The ATLAS detector has a three-level trigger system: Level 1 (L1), Level 2 (L2) and event filter (EF) level. The levels are staged, meaning that the next level refines the event selection from the previous level by applying more precise or additional requirements. The Level 1 trigger uses high transverse momentum muons, electrons, photons, jets, $\tilde{\chi}^0$ -leptons, large missing and total transverse energies for triggering. Only reduced detector information is used in order to make a decision with a latency shorter than $2.5\text{ }\mu\text{s}$. The rate is reduced from the Beam Cross Over (BCO) frequency of 40 MHz to 75 kHz (to be increased to 100 kHz in Run 2). The L1 trigger defines Regions Of Interest (ROI) that seed the L2 trigger. At L2, the full precision of all detector data in the ROI is used. The L2 trigger is configured to reduce the data rate to approximately 3.5 kHz with a latency less than 40 ms per event. At the EF level the data rate is further reduced to about 200 Hz for storage and offline analysis. The EF uses advanced near offline quality

algorithms for processing and requires around 4 seconds per event. The stored data size is approximately 1.3 Mbyte per event [102]. A schematic layout of the trigger system is shown in figure 4.7.

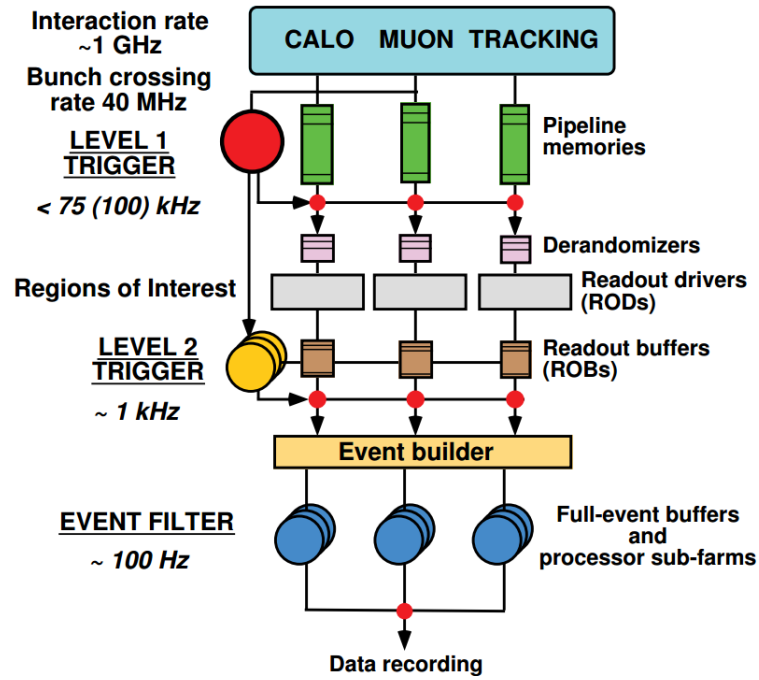


Figure 4.7: Schematics layout of the trigger system

Chapter 5

Charged Higgs boson search in ATLAS

5.1 Production and decay of charged Higgs boson

As discussed in previous chapters, the production mechanisms [28] and decay modes of a charged Higgs boson depend partly on its mass m_{H^\pm} . For light charged Higgs bosons ($m_{H^\pm} < m_{top}$, where m_{top} is the top-quark mass), the primary production mechanism is through the decay of a top quark, $t \rightarrow bH^\pm$. For $m_{H^\pm} > m_{top}$, the leading H^\pm production modes at the LHC are expected to be $gb \rightarrow tH^\pm$ (in a five-flavor scheme, or 5FS) and $gg \rightarrow tbH^\pm$ (in a four flavor scheme, or 4FS), i.e. in association with a top quark. In the 4FS, b quarks are dynamically produced, whereas in the 5FS, the b quark is also considered as an active flavor inside the proton. Diagrams illustrating the leading-order production mechanisms of interest for the current energy scale of the LHC are shown in figure 5.1.

As previously mentioned, $\tan\beta$ and the charged Higgs mass m_{H^\pm} are the key parameters which govern the decay properties. By constraining one, the branching ratio (BR) varies

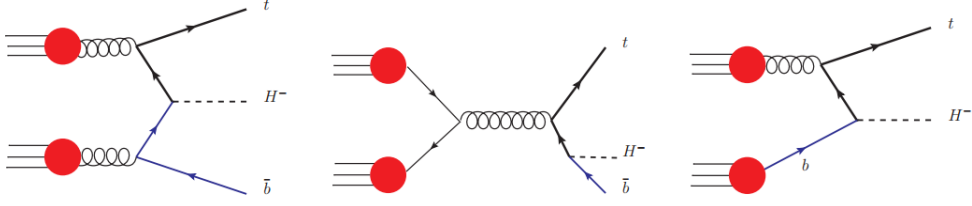


Figure 5.1: Example of leading-order Feynman diagrams for the production of a charged Higgs boson with a mass $m_{H^\pm} > m_{top}$, in 4FS (left and centre) and 5FS (right).

according to the other. In this manner the most significant decay channel can be found. By looking at figure 5.2, the top two decays are noticed immediately. For masses lower than 200GeV , the search for a charged Higgs should focus on the decay to $\tau\nu$. This ratio alters quickly as the mass increases above the top mass, allowing the creation of $t\bar{b}$ pairs. Thus, when searching for a "light" H^\pm , one would target the $\tau\nu$ channel, while for a "heavy" H^\pm , the channel of $t\bar{b}$ should become a prime choice.

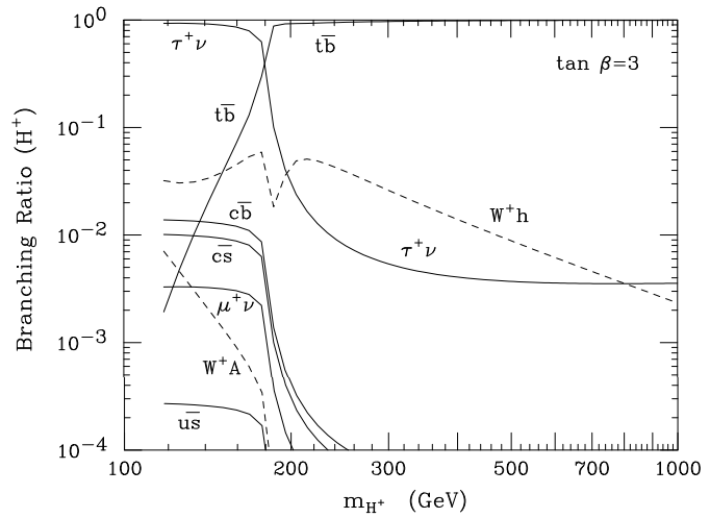


Figure 5.2: Branching ratios of the charged Higgs boson decay with $\tan\beta = 3$ as a function of the particle mass [30]

5.2 Data and simulation samples

5.2.1 Data samples

Only events recorded with all ATLAS sub-systems fully operational are used for this analysis. Together with the requirement of having 8 TeV pp collisions with stable beams, this results in a 2012 data sample of $20.3 \pm 0.6 \text{ fb}^{-1}$. The uncertainty on the integrated luminosity of 2.8 % is derived following the same methodology as that detailed in [70], from a preliminary calibration of the luminosity scale derived from beam-separation scans performed in November 2012.

Following basic data quality checks, further event cleaning is performed by demanding that no jet is consistent with having originated from instrumental effects, such as large noise signals in one or several channels of the hadronic end-cap calorimeter, coherent noise in the electromagnetic calorimeter, or non- collision backgrounds. In addition, events are discarded if the primary vertex (i.e. the vertex with the largest sum of track p_T^2) has fewer than five associated tracks with transverse momenta $p_T > 400 \text{ MeV}$.

In this analysis, events are triggered using unscaled single-lepton (electron or muon) triggers with the lowest available p_T threshold. By adding an **OR** condition with a second trigger that has a higher p_T threshold, one recovers some efficiency otherwise lost due to the isolation cuts in the triggers with lower thresholds.

5.2.2 Monte Carlo simulations

Monte Carlo (MC) simulated samples are used to develop and validate the analysis method in an unbiased way by not looking at the data up to the last stages of the analysis. By doing so the MC is used to calculate the signal selection efficiency and some background contributions ($t\bar{t}$ and single top-quark production, as well as $W + jets$, $Z/\gamma^* + jets$ and diboson events) and for the evaluation of systematic uncertainties. The MC samples used in this analysis are obtained with the ATLAS full GEANT4 simulation [69] and are reconstructed using the same analysis chain as the data.

The modelling of $t\bar{t}$ events is performed with POWHEG-BOX v2.0 [71, 72], using the CT10 [73, 74] parton distribution function (PDF) set. It is interfaced to PYTHIA v6.425 [75], with the Perugia P2011C [83] set of tuned parameters (tune) for the underlying event. The $t\bar{t}$ cross section at 8 TeV is $\sigma_{t\bar{t}} = 253_{-15}^{+13}$ pb for a top-quark mass of 172.5 GeV. It is calculated at next-to-next-to-leading order (NNLO) in QCD including resummation of next-to-next-to-leading logarithmic (NNLL) soft gluon terms with TOP++ v2.0 [76–82].

Samples of $t\bar{t}V$ ($V = W, Z$) are generated with the MADGRAPH v5 LO generator, with the CTEQ6L1 [84] PDF set. Parton shower and fragmentation are modeled with PYTHIA 6.425.

The single top-quark production is simulated using POWHEG (with the CT10 PDF set) interfaced to PYTHIA (with the CTEQ61L PDF set and the Perugia2011C underlying event tune). The cross sections are normalised to the approximate NNLO theoretical

predictions of [85–87]. Interference between SM $t\bar{t}$ and Wt processes is avoided using the diagram removal scheme [88].

For the simulation of W/Z +jets backgrounds, ALPGEN v2.14 [89], interfaced to PYTHIA, is used for the matrix-element calculation and the parton-shower evolution, with the CTEQ6L1 PDF set. To avoid double-counting of partonic configurations generated by both the matrix-element calculation and the parton-shower evolution, a parton-jet matching scheme (MLM matching) is employed. The MLM matching is applied inclusively for the production of W/Z + five partons and exclusively for the lower multiplicity sub-samples. The vector boson production with additional heavy-flavor partons ($W+c$, $W/Z+c\bar{c}$, $W/Z+b\bar{b}$) is simulated separately with ALPGEN. The inclusive W and Z/γ^* production samples are formed by adding the corresponding parton multiplicity sub-samples including both the "light-quark-with-jets" and the "heavy-quarks-with-jets" processes with the relevant cross sections. The Heavy-Flavor Overlap Removal (HFOR) tool [90] is used to avoid double counting in the heavy-quark generation. The samples are normalised to the inclusive NNLO theoretical cross section [91]. These are also reweighted to account for the difference of the W/Z p_T spectrum between data and simulation [92].

Finally, diboson events (WW , WZ and ZZ) are produced using ALPGEN v2.14, interfaced to HERWIG v6.520 [93], for the matrix-element calculation and the parton-shower evolution, with the CTEQ6L1 PDF set. The samples are generated with up to three additional partons and are normalised to their NLO theoretical cross sections [94]. In order to cover also the $\ell\nu qq$ final state of the WZ production, additional SHERPA samples were used for both the matrix-element calculation and the parton-shower evolution, with the

CT10 PDF set. The samples are also generated with up to three additional partons and the cut $p_T > 25$ GeV is imposed on the lepton.

In addition to the MC samples described above, events with a Higgs boson are also considered as a background in this analysis. Due to the high number of jets and b jets in the analysis, the most relevant background consists of events with a Higgs boson produced in association with top quarks. The dominant decay of the Higgs boson (at $m_H = 125$ GeV) is $H \rightarrow b\bar{b}$. The $t\bar{t}H$ process is modeled using matrix elements obtained from the HELAC-ONELOOP package [95] that corresponds to the NLO QCD accuracy. POWHEG-BOX [96, 97] is the interface to the parton shower. The samples created using this approach are referred to as PowHel samples. The top-quark mass is set to 172.5 GeV. The cross section for $t\bar{t}H$ and the Higgs boson decay branching ratios are taken from the NLO theoretical calculations of Ref. [98].

All SM background samples derived from simulations are scaled such that the total number of events corresponds to the recent theoretical predictions on the cross sections at NLO or NNLO [99] in compliance with [24]. Where applicable, Tauola [100] is used for the τ decays and Photos [101] is employed for photon radiation from charged leptons. The event generators are tuned in order to describe the ATLAS data. The Perugia tune P2011C [102] is used for events for which the hadronization is simulated with Pythia (except for the AcerMC $t\bar{t}$ datasets, where the tune AUET2B [103] is used), while the tune AUET2 [104] is used for Herwig. Finally, all MC events are overlaid with additional minimum bias events generated with Pythia to simulate the effect of multiple pp collisions per bunch crossing (pile-up), at a variable rate. The simulated events are then weighted [116]

to the same number of collisions per bunch crossing as the data.

For the signal samples, with a charged Higgs boson mass between 200 and 600 GeV, simulated events of top-quark associated H^\pm production are produced with POWHEG, using the CT10 NLO PDF set, interfaced with PYTHIA 8. For the $H^\pm \rightarrow tb$ decay, PYTHIA 8 was used and a one-lepton filter (with no p_T cut at the truth level) was subsequently applied for the W -boson decays, in order to eventually select lepton+jets events only. Since the experimental resolution is much larger than the natural width of the charged Higgs boson and in order to study model-independent H^\pm production, the width in all signal samples was set to 0 for the production.

5.3 Event Selection

In the events selected for this analysis, the top quarks both decay via $t \rightarrow Wb$, where one W boson decays hadronically and the other decays into an electron or a muon, either directly or through a τ -lepton decay, and the corresponding neutrino(s). The signal event signature is therefore characterized by the presence of exactly one high p_T charged lepton (electron or muon) and five or more jets, at least three of them being b -tagged as displayed at figure 5.3.

Events collected using either an isolated or non-isolated single-lepton trigger are considered. Isolated triggers have a threshold of 24 GeV on p_T for muons and on E_T for electrons, while non-isolated triggers have higher thresholds at 36 GeV (muons) and 60 GeV (electrons). The isolated triggers have a loss of efficiency at high p_T or E_T , which is recovered by the triggers with higher thresholds. For reasons of region categorization

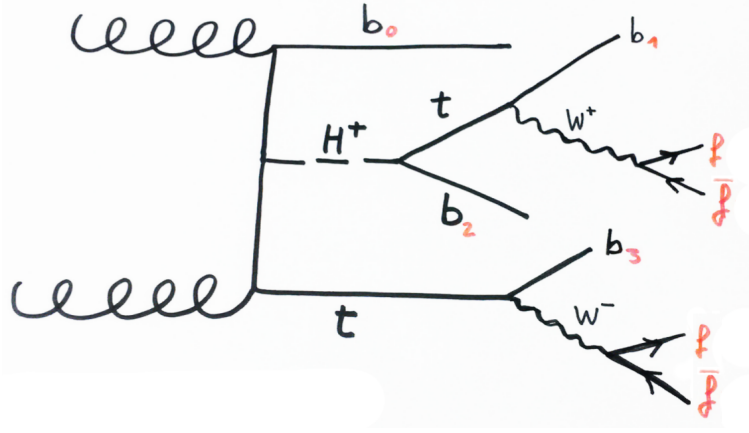


Figure 5.3: Feynman diagram of H^\pm decaying into tb pair, resulting in six jets, of which four are b -jets with the remaining jets originating from the hadronic decay of one W boson while the other decays leptonically.

Events accepted by the trigger are then required to have exactly one identified electron or muon, and at least four jets, of which at least two must be identified as b -tagged jets. The selected lepton is required to match, with $\Delta R < 0.15$, a lepton reconstructed by the trigger.

5.3.1 Objects reconstruction

5.3.1.1 Electrons

Electrons are reconstructed by matching clustered energy deposits in the electromagnetic calorimeter to tracks reconstructed in the inner detector [105]. Candidates are required to meet quality requirements based on the shower shape [106]. The transverse energy $E_T = E_{clus}/\cosh(\eta_{track})$, computed using the calorimeter cluster energy E_{clus} and the direction of the electron track η_{track} , is required to be larger than 25 GeV. The pseudorapidity range for the electromagnetic cluster covers the fiducial volume of the detector, $|\eta| < 2.47$

(the transition region between the barrel and end-cap calorimeters, $1.37 < |\eta| < 1.52$, is excluded). Same as the Muons, z_0 must be smaller than 2 mm. In addition, E_T and η -dependent calorimeter (tracking) isolation requirements are imposed in a cone with a radius $\Delta R = 0.2$ around the electron position, with an efficiency of about 90% for true isolated electrons [107, 108]. The efficiencies of the electron trigger, reconstruction and identification are measured using $Z \rightarrow ee$ and $W \rightarrow e\nu$ events, in both data and MC samples. Simulations are generally found to model the data well, with a few exceptions, mainly regarding the lateral development of showers and the TRT in the end-caps. Scale factors are derived to parametrise efficiency differences between data and simulations. Control plots for p_T and η of the electrons are shown in figure 5.4.

5.3.1.2 Muons

Muon candidates are required to contain matching inner detector and muon spectrometer tracks [66, 67] as well as to have $p_T > 25\text{GeV}$ and $|\eta| < 2.5$. Combined and tight muons, with z_0 (the longitudinal impact parameter z_0 of the electron track relative to the primary vertex) smaller than 2 mm, as well as a good track quality [68], are selected. Only isolated muons are accepted by requiring that the scalar sum of the track p_T in a cone of a variable radius, defined by $\Delta R < 10\text{GeV}/p_T^\mu$ around the muon (while excluding the muon track itself) be less than 5% of the muon transverse momentum p_T^μ . Control plots for p_T and η of the muons are shown in figure 5.5.

5.3.1.3 Jets

Jets are reconstructed from topological clusters in the calorimeters using the anti-kt algorithm [109, 110] with a size parameter value of $R = 0.4$. A local calibration is ap-

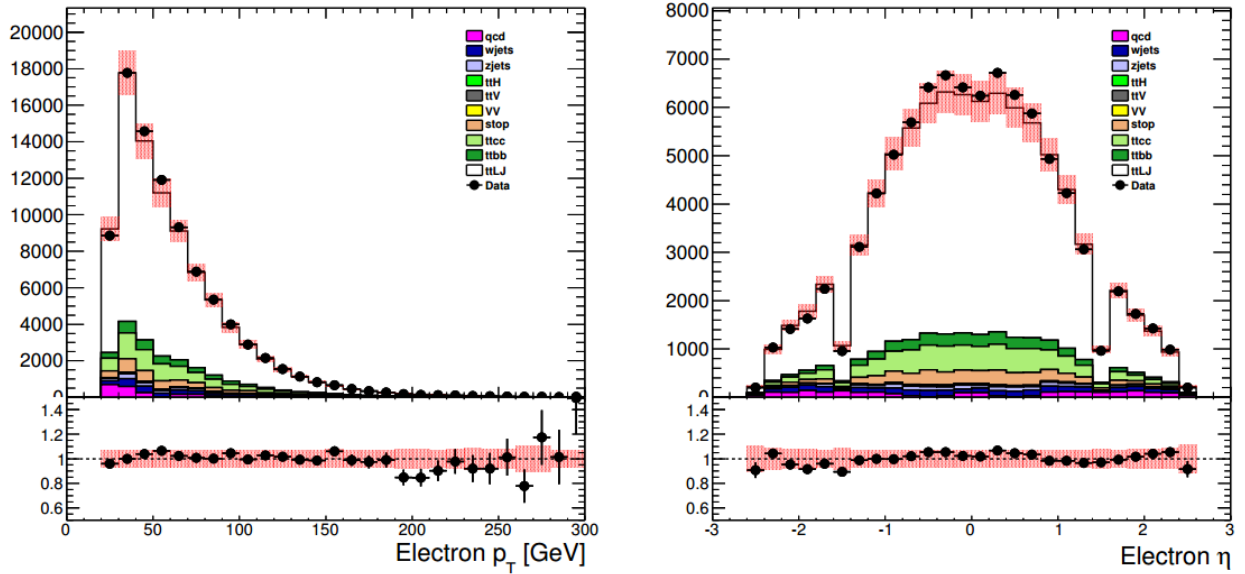


Figure 5.4: Comparison between the data and the simulated SM processes for the electron p_T (left) and η (right) in events with four jets and two b jets. The data are shown as points with error bars and compared to the sum of all expected contributions taken from simulations (t +LF, tt +HF, $tt + W/Z$, W +jets and others as Z +jets, single top, di-boson and $t\bar{t}H(\rightarrow b\bar{b})$). The red shaded region corresponds to the systematic error due to uncertainties on the cross sections. Presented below is the ratio plot between the data and monte-carlo events as a measure to deviations.

plied [111, 112], which reduces fluctuations due to the non-compensating nature of the calorimeters, dead material and out-of-cluster leakage. Calorimeter clusters are classified as either electromagnetic or hadronic by considering properties such as the energy density of the cluster, isolation and shower depth in the calorimeters. Corrections, derived from simulations and based on jet areas [113], are then applied in order to reduce the effects of pile-up on the jet calibration [114]. Only jets with a transverse momentum $p_T > 25\text{GeV}$ and a direction within $|\eta| < 2.5$ are considered in the following. A method that allows for the identification and selection of jets originating from the hard-scatter interaction through the use of tracking and vertexing information is used [114]. This is referred to

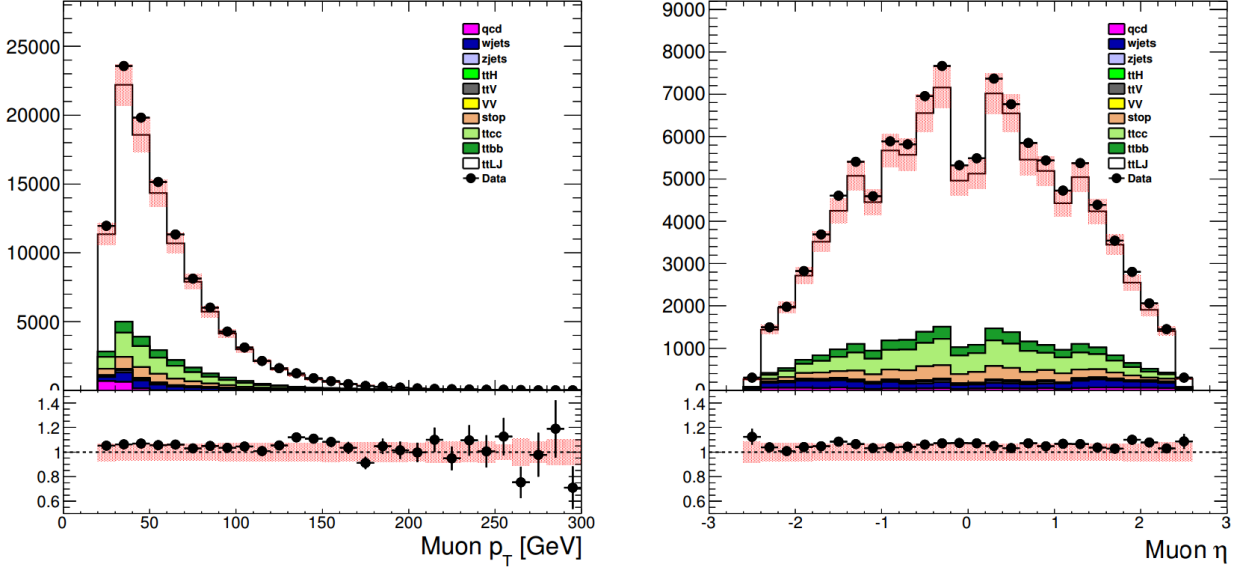


Figure 5.5: Comparison between the data and the simulated SM processes for the muon p_T (left) and η (right) in events with at least four jets and at least two b jets. The data are shown as points with error bars and compared to the sum of all expected contributions taken from simulations (t +LF, tt +HF, $tt + W/Z$, W +jets and others as Z +jets, single top, di-boson and $t\bar{t}H(\rightarrow b\bar{b})$). The red shaded region corresponds to the systematic error due to uncertainties on the cross sections. Presented below is the ratio plot between the data and monte-carlo events as a measure to deviations.

as the "Jet Vertex Fraction" (JVF), defined as the fraction of the total momentum of the charged particle tracks associated to the jet which belongs to tracks that are also compatible with the primary vertex (pv):

$$JVF(jet_i, pv) = \frac{\sum_k p_T(trk_k^{jet_i}, pv)}{\sum_n \sum_l p_T(trk_l^{jet_i}, vtx_n)} \quad (5.1)$$

The jet selection based on this discriminant is shown to be insensitive to pile-up. If no tracks are matched to a jet, a JVF value of -1 is assigned. In this analysis, $|JVF| > 0.5$ is required for jets with $p_T < 50$ GeV and $|\eta| < 2.4$ since pile-up jets are expected to be soft. In order to identify the jets initiated by b quarks, the MV1 algorithm is used, which

combines impact-parameter information with the explicit determination of an inclusive secondary vertex [115]. MV1 is a neural network-based algorithm using the output weights of the various b -tagging algorithms. A working point is chosen that corresponds to an average efficiency of 70% for b -jets in $t\bar{t}$ events (corresponding to a weight $\omega_{MV1} > 0.7892$). Tagging and mis-tagging efficiency scale factors relate efficiencies as determined in various data samples to their counterparts in simulation. They are used in all simulated events, after having applied the b -tagging algorithm to the jets. Note that the b -tagged jets are required to pass the same p_T , η and JVF selection as all other jets. An example of control plots for p_T and η of the leading jet is shown in figure 5.6.

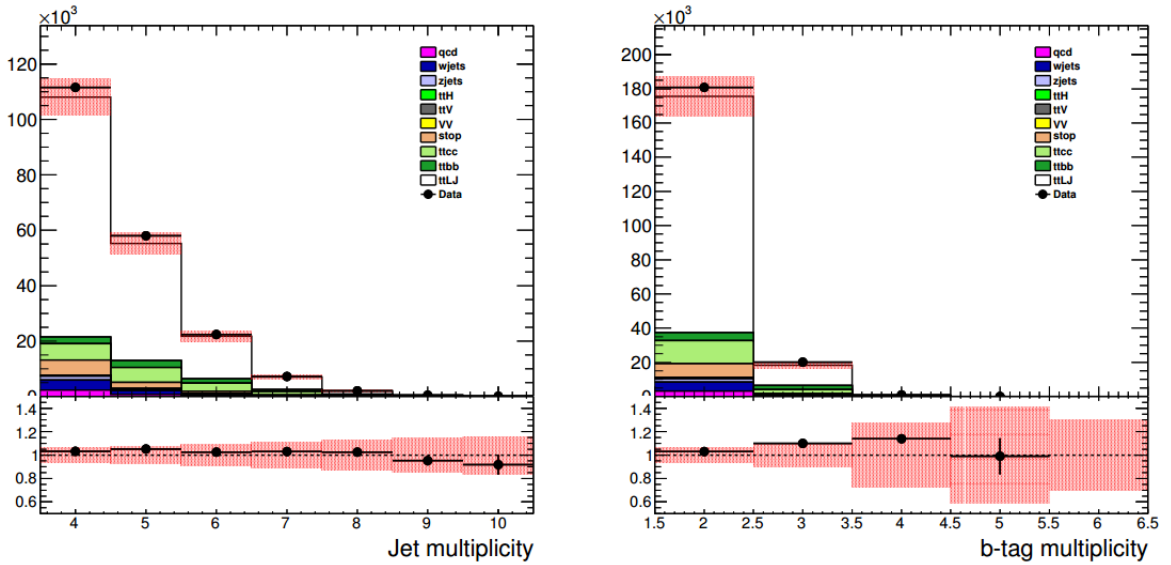


Figure 5.6: Comparison between the data and the simulated SM processes for the jet multiplicity (left) and the b -jet multiplicity (right) for all events with at least 4 jets and at least 2 b -tags. The data are shown as points with error bars and compared to the sum of all expected contributions taken from simulations (t +LF, tt +HF, $tt + W/Z$, W +jets and others as Z +jets, single top, di-boson and $t\bar{t}H(\rightarrow b\bar{b})$) or estimated using a data-driven technique (misidentified leptons). The red shaded region corresponds to the systematic error due to uncertainties on the cross sections. Presented below is the ratio plot between the data and monte-carlo events as a measure to deviations.

5.3.2 Charged Higgs boson selection

Since this analysis relies on reconstructing two top-quark candidates in the final state, the event sample is obtained by following the standard single-lepton $t\bar{t}$ selection cuts, which are described in [118]. In order to account for the high jet multiplicity in signal events, two additional cuts on the jet and b -jet multiplicities have been applied at the end of the selection chain. In the following, we refer to the sample with ≥ 5 jets and ≥ 3 b jets as the signal region. The regions with 4 jets and ≥ 2 b jets, as well as the regions with 5 or 6 jets with exactly 2- b jets, are considered as the control regions. The remaining regions with ≤ 2 b jets are not considered in the analysis. The selection is as follows:

- The appropriate single-electron or single-muon trigger has fired.
- The event contains at least one primary vertex with more than four good tracks.
- The event contains exactly one reconstructed lepton (e/μ) with $p_T > 25$ GeV that has been matched to the corresponding high-level trigger object (within $\Delta R < 0.15$). Double counting of the two trigger streams is taken care of.
- Additionally, no lepton of the other flavour must be found.
- The event is required to have at least four jets with $p_T > 25$ GeV, $|\eta| < 2.5$ and a jet vertex fraction (JVF) with respect to the primary vertex of $|\text{JVF}| > 0.5$ for jets with $p_T < 50$ GeV and $|\eta| < 2.4$.
- At least one of the selected jets needs to be tagged by the MV1 algorithm ($w_{\text{MV1}} > 0.7892$ corresponding to an average b -tagging efficiency of $\epsilon_b = 70\%$).

- In addition to the $t\bar{t}$ selection described above, additional cuts are applied in the signal region:
 - at least five jets with $p_T > 25$ GeV;
 - at least three of them have to be b -tagged jets.

5.3.2.1 Categorization

The categories used in the analysis, according to $\text{jet}(j)$ and $b\text{-jet}(b)$ multiplicity:

- Control region $4j2b$ (CR42)
- Control region $5j2b$ (CR52)
- Control region $6j2b$ (CR62)
- Control region $4j \geq 3b$ (CR43)
- Signal region $\geq 5j \geq 3b$ (SR)

The event yields for data and all individual Monte Carlo simulations are presented in table 5.1 using the direct b -tagging. The event yields are normalized to an integrated luminosity of 20.3 fb^{-1} . A good agreement between data and simulation is found in the control regions.

Process	CR42	CR52	CR62	CR43	SR
ttbb	$1718.3^{+934.3}_{-935.9}$	$1549.7^{+828.8}_{-830.5}$	$1386.5^{+822.3}_{-823.6}$	664.8 ± 372.4	$2259.8^{+1137.3}_{-1139.8}$
ttcc	$5201.7^{+2918.6}_{-2923.7}$	$4460.3^{+2560.2}_{-2564.5}$	$3833.6^{+2326.1}_{-2329.7}$	735.6 ± 410.5	$1828.9^{+920.5}_{-922.4}$
ttLJ	$80299.2^{+9698.2}_{-10062.2}$	$38707.8^{+7385.6}_{-7496.4}$	$19290.4^{+5243.7}_{-5282.7}$	$6262.9^{+1010.4}_{-1032}$	$5647.2^{+323.6}_{-373.9}$
ttH	33.7 ± 4.2	$44.6^{+4.8}_{-6}$	$68.9^{+8.2}_{-10}$	15.5 ± 2.4	$87.1^{+8.1}_{-10.9}$
ttV	127.9 ± 40.1	150.9 ± 46.6	188.8 ± 59.2	17.6 ± 5.7	85.2 ± 25.7
stop	$5014.6^{+775.9}_{-758.8}$	$1966.8^{+417.1}_{-412.7}$	875.3 ± 270.5	364.8 ± 83.6	$327.4^{+18.8}_{-16}$
wjets	3402.4 ± 1714.5	1269.5 ± 717.1	638 ± 395.5	188.2 ± 99.8	173.1 ± 93
zjets	1330.7 ± 671	397.3 ± 224.2	152.5 ± 95.2	53 ± 30.7	48.8 ± 26.2
VV	231.7 ± 69.4	107.5 ± 41.3	51.9 ± 25.3	10.7 ± 3.7	13.7 ± 4.7
qcd	2156.9 ± 865.5	666 ± 264.2	334.6 ± 152.4	157.9 ± 67.5	153.4 ± 57.3
total	$99930.6^{+11269.4}_{-11637.9}$	$49658.6^{+8500.9}_{-8628.8}$	$27069.9^{+6562.8}_{-6613.1}$	$8660.7^{+1318.3}_{-1343.1}$	$11122.5^{+1578.7}_{-1612.4}$
Data	102462 ± 320.1	51421 ± 226.8	26948 ± 164.2	9102 ± 95.4	11945 ± 109.3

Table 5.1: Prefit event yields of MC and data in the five categories used in the analysis. The numbers for the expected backgrounds do include all uncertainties, and the uncertainties on the data are simply the sqrt.

5.4 Backgrounds

5.4.1 $t\bar{t}$ heavy flavour classification

The production of $t\bar{t}$ together with heavy flavours (such as pairs of b or c quarks) is connected to large uncertainties. An example Feynman diagram for this sort of background is depicted in figure 5.7. The $t\bar{t}$ sample is classified into tt+light, tt+bb and tt+cc sub samples, based on the truth record. This so-called heavy flavour classification is following

exactly the same prescription defined by $t\bar{t}H$, $H \rightarrow b\bar{b}$ [92]: All particle jets with $p_T > 15$ GeV and $|\eta| < 2.5$ which are matched using a $\Delta R < 0.4$ to a b -hadron not originating from a top quark with $p_T > 5$ GeV are labelled as b . If the event has one or two matches to such a particle jet, or if the event has one such particle jet which is matched to two b -hadrons, then the event is classified as $t\bar{t}+b\bar{b}$. The same procedure is repeated for c jets if no b -hadron not-from-top match is found. All other events are labelled as $t\bar{t}$ +light events.

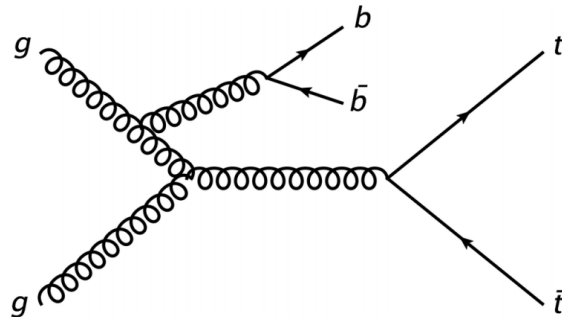


Figure 5.7: Example diagram for the $t\bar{t}b\bar{b}$ process.

5.4.2 Background composition

A good description of the physics background is crucial for this analysis. One has to understand the background accurately in order to claim or dismiss an excess of events in the signal regions. Studying the background composition helps finding control regions for the various contributions and to better constrain them using data.

Preselected events are categorised according to the number of jets with $p_T > 25$ GeV and the number of b -tags. The separation of the event samples with a higher signal-to-background ratio from the ones dominated by particular backgrounds allows use of

the data to constrain the related systematic uncertainties in the control (signal-free) regions. Using MC simulations at $\sqrt{s} = 8$ TeV normalised to 20.3 fb^{-1} , the background composition is shown in figure 5.8. The most problematic background is the $t\bar{t}b\bar{b}$, because it has the most and also the largest uncertainties. Unfortunately, the amount of $t\bar{t}b\bar{b}$ in the four control region is rather small, so it is not possible to effectively constrain it. Only the signal region itself can be used to get a handle on that background. This is achieved by training a BDT against only this $t\bar{t}b\bar{b}$ background, which is described in detail in Section 5.5.

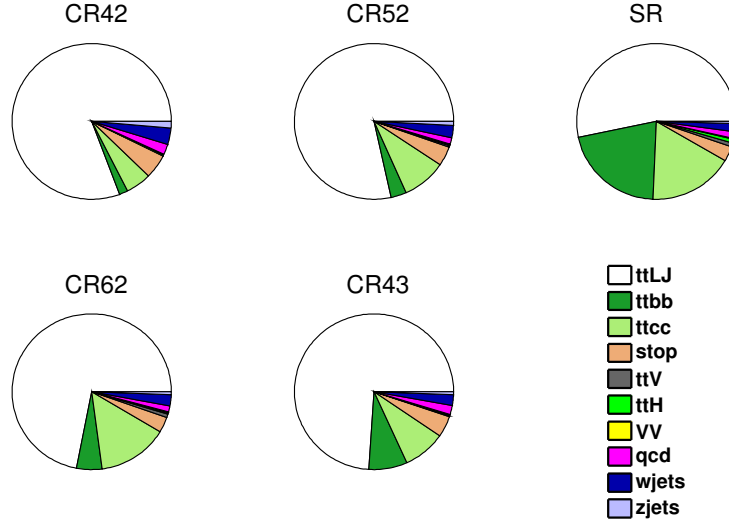


Figure 5.8: Background composition for the five categories. The dominant background is $t\bar{t}$ +light jets. In the SR significant contributions of $t\bar{t}b\bar{b}$ and $t\bar{t}c\bar{c}$ are expected.

5.5 Signal and background separation using Boosted Decision Trees

The classification of events is one of the main challenges that HEP analysis is facing. To claim a discovery, one needs to reject the null-hypothesis, which in this case consists of a SM background. Lacking a perfect discriminating variable, each cut may discard both signal and background. This is a classic *classification* problem. The field of Machine-Learning (ML) deals with these cases and provides promising solutions and approaches with the purpose of minimising the loss of signal. Given a set of training cases/objects and their attribute values, the goal is to determine the target class value of new examples. In HEP terms, this is a search of a generic way to distinguish data from background according to event's properties, both raw (measured by the detector) and derived (calculated by physicists).

5.5.1 Decision trees and boosting

Decision Trees are considered to be one of the most popular approaches for representing classifiers. A decision tree is a binary tree structured classifier. A single decision tree is trained on a Monte Carlo simulation sample of known composition and tested on an independent known sample. All provided variables are scanned at each step to find the single cut which best separates signal from background according to a chosen metric. The sample is divided by the chosen cut and the algorithm is applied again on each resulting sub-sample. This sample splitting continues until a stopping condition is reached, usually the minimum number of events allowed in a sub-sample (minimum leaf size). Hence, a

single decision tree makes a series of cuts, but does not discard events: an event which fails a given cut continues to be considered by the algorithm. The algorithm divides up the space into signal-like and background-like regions and it assigns a score to each event depending on which region it falls into.

”Boosting” is a common method to improve the performance and stability of decision trees. After the first tree is trained, events are weighted such that those mis-classified by the first tree have their weights increased. A second tree is then trained on this re-weighted sample and naturally focuses on the events which were problematic in the first tree. This is a single “boost”. The number of boosts is a parameter to be optimised. At the end of the boosting cycle, a score is assigned to each event using a weighted average of the score calculated in each tree. The weight used is derived from the mis-classification rate of each tree.

The training parameters of the BDT must be optimised to yield the best performance on unseen events in a withheld test set. It is easy to achieve any level of performance (even perfect classification) on the training set, but this certainly does not imply good performance on an independent test set where the performance can degrade (this is referred to as over-training). The training parameters must therefore be optimised according to the performance on an independent test set.

A BDT makes use of a set of discriminating variables. The chosen variables should be well-modelled by the training samples (Monte Carlo simulations) and provide some signal discrimination against the background. Furthermore, the input variables should be as uncorrelated as possible. A large number of variables were considered. From those, a short list was chosen, based upon their discrimination power and BDT performance. The variables were selected using an iterative method. The list of variables was divided

into several subsets and the best variables from these subsets were further evaluated to trim down the list. Since there are large differences in kinematics between the H^\pm 200 GeV mass point and the 600 GeV mass point, best variables at these two end points were selected and merged into a single list. The variables selected from this combination procedure are used across the entire mass range.

5.5.2 Input variables

The variables used for the BDT training, along with a short description, are shown in Table 5.2.

Value	Definition
ave_dRb	Average $\Delta R(b, b)$ between two b-jets in the event
W2	Second Fox-Wolfram moment $\sum_{i,j} \frac{ p_i p_j }{E_{vis}^2} P_2(\cos\theta_{ij})$
H_T^{Had}	Scalar sum of p_T in the event
minR_Mbb	Invariant mass of the two b-jets that are closest in ΔR
jet1pt	Leading jet p_T

Table 5.2: Variables entering the BDT training.

Figures 5.9 - 5.11 display the control region validation of the input variables.

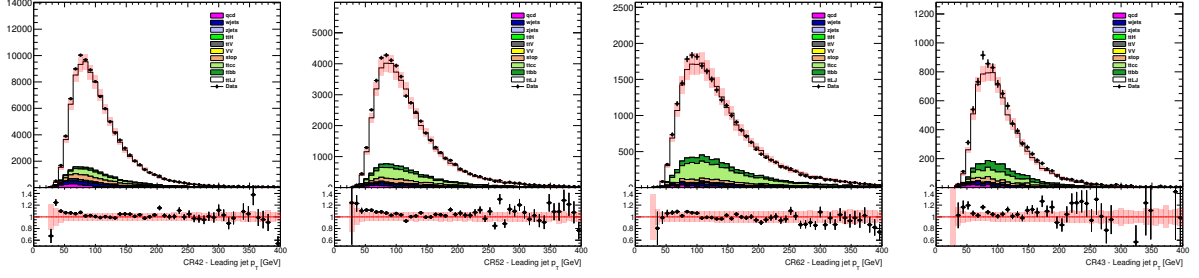


Figure 5.9: Prefit data to MC comparison for the leading jet p_T in the four control regions, as indicated in the labels. The red shaded bands indicate the cross section uncertainties. Both e and μ channels are summed up here.

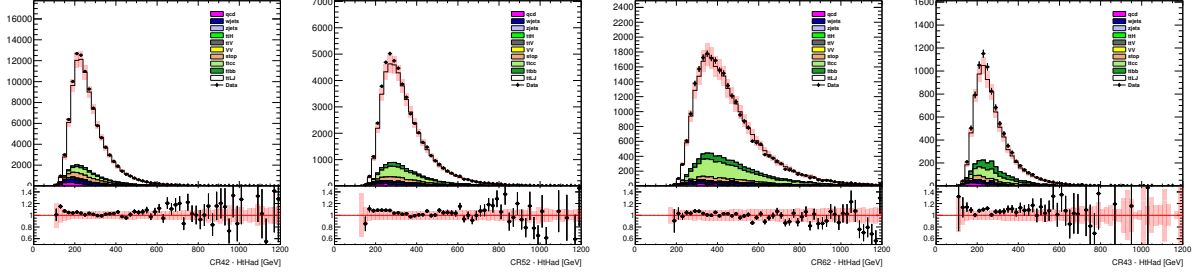


Figure 5.10: Prefit data to MC comparison for the H_T^{HAD} in the four control regions, as indicated in the labels. The red shaded bands indicate the cross section uncertainties. Both e and μ channels are summed up here.

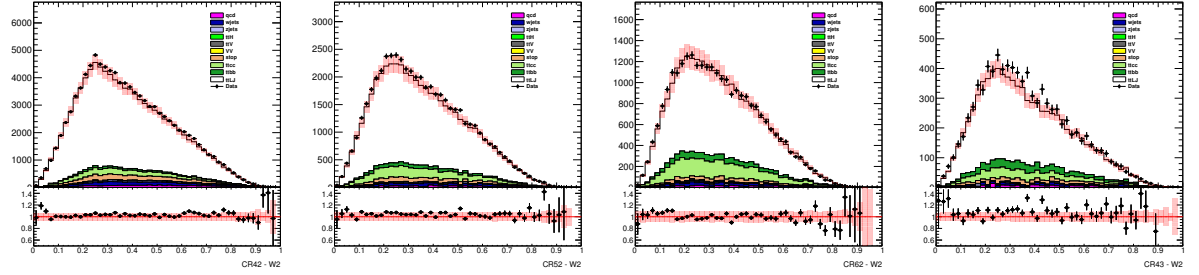


Figure 5.11: Prefit data to MC comparison for the second Fox Wolfram moment in the four control regions, as indicated in the labels. The red shaded bands indicate the cross section uncertainties. Both e and μ channels are summed up here.

5.5.3 Heavy Flavour BDT

A crucial point in MVA training (sometime neglected) is the selection of background composition. If a particle such as H^\pm exist, a deviation of the data from the entire background composition is expected. With that in mind, an obvious choice is taking all of the analysis backgrounds to train against (as described in section 5.4.2). Seeing that not all backgrounds in this analysis have the same properties, care must be taken in this step.

Heavy Flavour (HF) BDT was designed in an attempt to reduce the strong anti-correlation between $t\bar{t}b\bar{b}$ (the background with the most uncertainties, including the largest ones) and H^\pm . This BDT was validated thoroughly, cross checked against an inclusive (all backgrounds) BDT, and found to be more sensitive to signal events. The code framework used was Tool for Multi Variate Analysis (TMVA) 4.2.0 [117]. The samples were divided into two, half for the training and second half for the the testing of the HF BDT according to their MC event number.

The discrimination from background and signal by the input variables entering the HF BDT is presented for a mass hypothesis of 250 GeV in figure 5.12 and for a mass of 500 GeV in figure 5.13. By comparing the BDT output using the events in the training sample to those in the test sample one can check for potential overtraining effects. This test is displayed for all mass hypotheses in figure 5.14. No overtraining is observed.

An important step in training a MVA is validating the control regions. Since the BDT trained for "finding" signal events at the signal region, it should provide a fine compliance

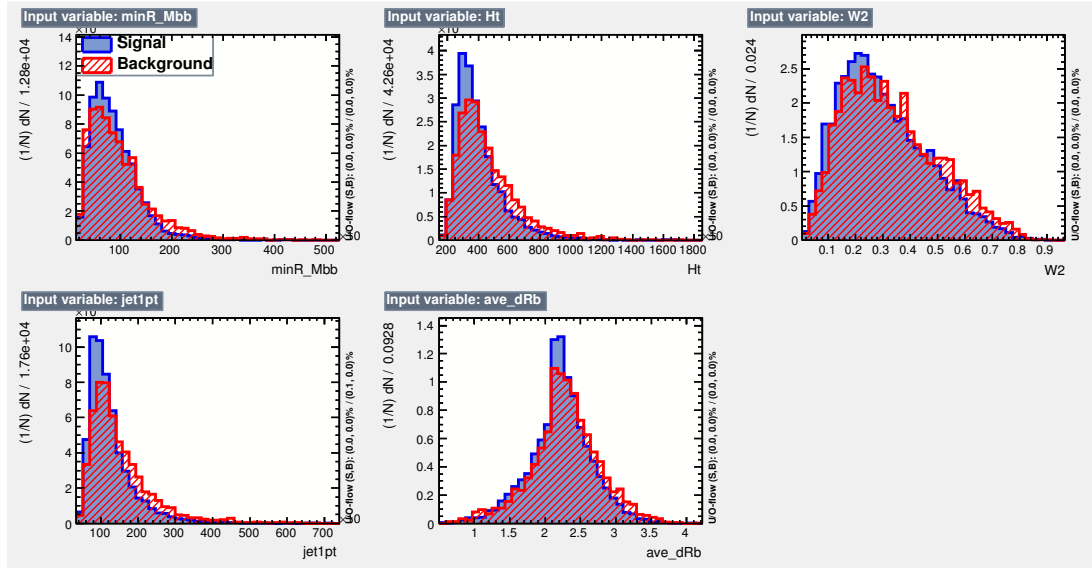


Figure 5.12: The input variables used for the HF BDT training, here for the signal of 250 GeV.

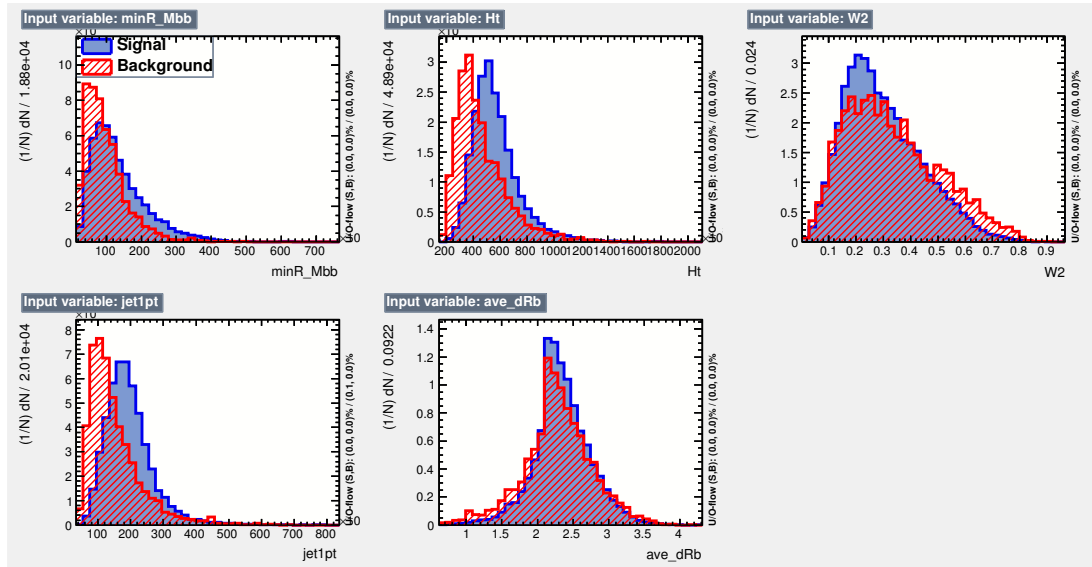


Figure 5.13: The input variables used for the HF BDT training, here for the signal of 500 GeV.

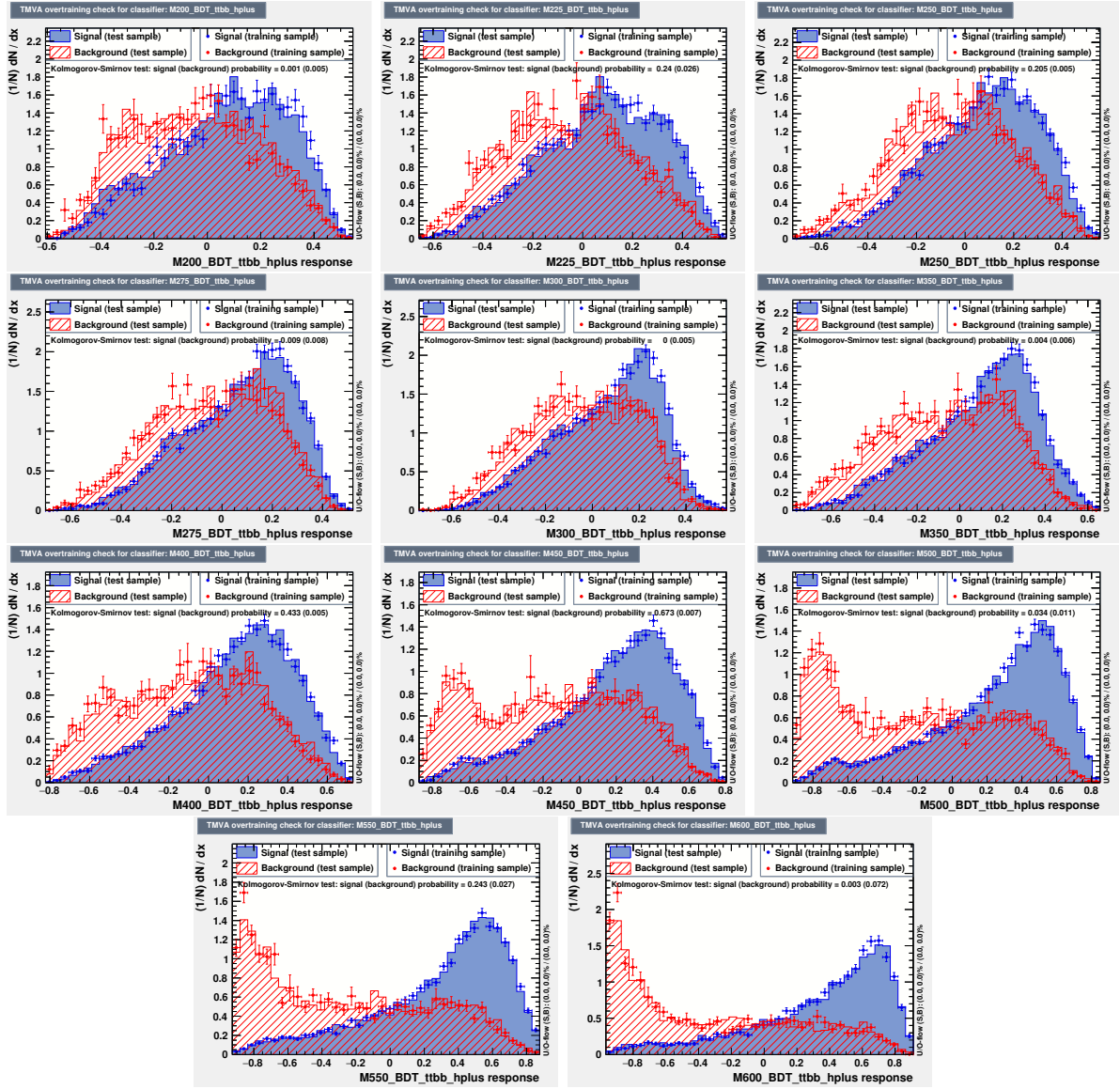


Figure 5.14: BDT output and overtraining check for the HF BDT trained for all 11 signal hypotheses, as indicated in the x-axis label.

between MC and data at the control regions. In figures 5.15-5.17 the validation of the HF BDT in the control regions is shown for three mass points: 250 GeV, 300 GeV and 450 GeV. A good agreement is observed for all mass points and all categories.

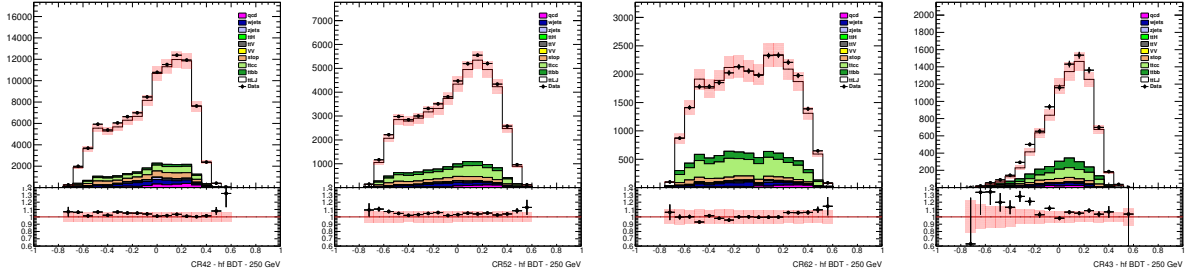


Figure 5.15: Data-MC comparison of the HF BDT output in the four control regions, for the training against a signal with a mass of 250 GeV.

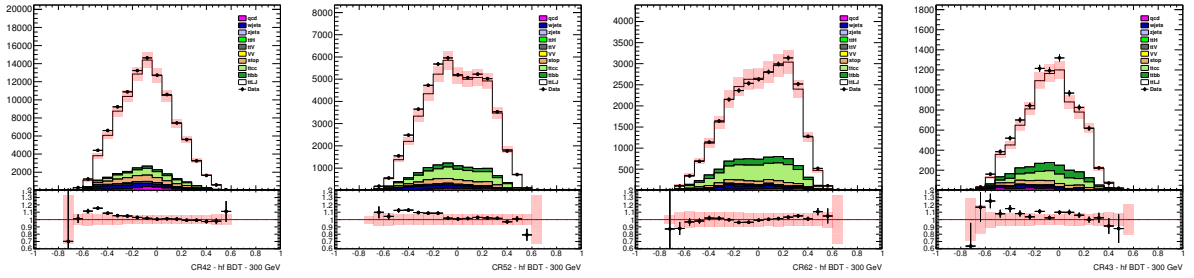


Figure 5.16: Data-MC comparison of the HF BDT output in the four control regions, for the training against a signal with a mass of 300 GeV.

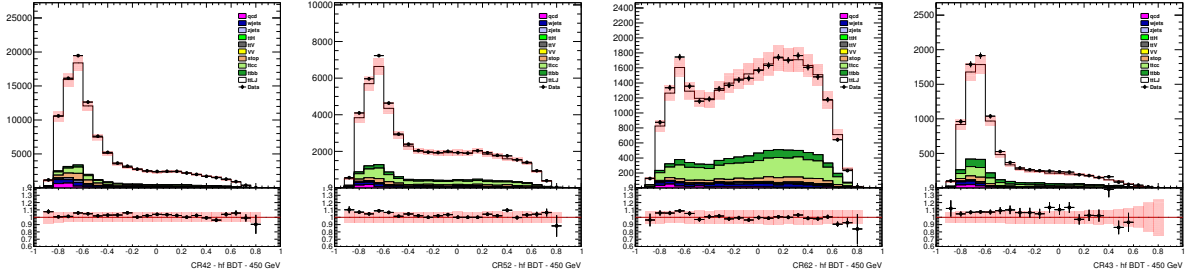


Figure 5.17: Data-MC comparison of the HF BDT output in the four control regions, for the training against a signal with a mass of 450 GeV.

5.6 Systematic uncertainties

5.6.1 Uncertainties on Physics Objects

Luminosity

The uncertainty on the measured integrated luminosity is 2.8 % [119]. This systematic uncertainty is applied to all contributions determined from MC simulations.

Leptons

The uncertainties for the lepton selection are connected to trigger, reconstruction, identification, isolation and lepton momentum scale and resolution. In total 5 (6) components of uncertainties are considered for electrons (muons).

The reconstruction as well as the identification and trigger efficiencies are slightly different in data and simulations. To correct accordingly, scale factors are derived by using tag-and-probe methods based on $Z \rightarrow \ell\ell$ ($\ell = e/\mu$) data and simulation samples. The total uncertainties on the event yields from the lepton reconstruction are 1.3 % for the single lepton selection channel. The lepton momentum scale and resolution are tested using the reconstructed distributions of the $Z \rightarrow \ell\ell$ and $J/\Psi \rightarrow \ell\ell$ masses. Small discrepancies are observed between data and simulations and corrections are applied in the latter.

Jet Energy Scale

The jet energy scale (JES) and the corresponding uncertainties are derived from test-beam data, LHC collision data and simulations [120–124]. The JES uncertainty is split up into 22 uncorrelated sources with different dependencies on p_T and η and are treated as uncorrelated in this analysis.

Jet Vertex Fraction

The efficiency of the jet vertex fraction (JVF) requirement is measured per jet in data and simulation using $Z \rightarrow \ell\ell+1$ -jet events. The corresponding uncertainty is evaluated and propagated to the analysis by varying the nominal JVF cut value.

Jet Energy Resolution

The jet energy resolution (JER) is measured separately for data and simulation [120] and the systematic uncertainty is defined as the difference in quadrature. To quantify the corresponding systematic uncertainty in the analysis, the energy of the jet in simulation is smeared by this residual difference and the changes in the normalisation and shape of the final discriminant are compared to the default prediction.

Jet Reconstruction

The jet reconstruction efficiency is found to be $\approx 0.2\%$ lower in the simulation than in data for jets with $p_T < 30$ GeV and consistent with data for jets with p_T above. The jet- p_T cut for this analysis is at 25 GeV, accordingly 0.2% of the jets with $p_T < 30$ GeV are randomly removed and all jet-related variables are recomputed.

Flavour Tagging

The uncertainties of flavour tagging is evaluated for each jet flavour using control samples in data and compared to simulations. Corresponding scale factors and their uncertainties are derived to correct the per-jet tagging rates in simulations as a function of p_T . For the b -jets, the scale factors have been derived from a $t\bar{t}$ sample [125], whereas for c -jets events with identified D^* are used [126]. In the case of light jet flavours, the scale factors and their uncertainties are derived from di-jet events and are parameterized additionally in η [127]. An additional extrapolation uncertainty is applied on the b -tagging efficiency of high p_T jets.

A total of seven (four) independent sources of uncertainties affecting the b - (c -) tagging efficiencies are considered. Each of these uncertainties correspond to an eigenvector resulting from diagonalizing the matrix containing the information of total uncertainty per p_T bin and the bin-to-bin correlation. Twelve uncertainties are considered for the light jet tagging depending on the jet p_T and η . All flavour tagging systematics are taken as uncorrelated between b -, c -and light-flavour jets.

5.6.2 Uncertainties on Background Modeling

$t\bar{t}b\bar{a}$

- Inclusive cross section: The uncertainty is $+5\%/ -6\%$, this one is described by one NP and it acts on $t\bar{t} + \text{light}$, $t\bar{t}c\bar{c}$ and $t\bar{t}b\bar{b}$.
- $t\bar{t}$ reweighting: The nine largest uncertainties associated with the experimental measurement of top quark $t\bar{t}$ system p_T are considered as separate uncertainty sources

in the reweighting applied to the MC simulations. Given that the measurement is performed for the inclusive ttbar sample and the size of the uncertainties applicable to the tt+cc component is not known two additional uncertainties are assigned to tt+cc events corresponding to the ttbar pT and top quark pT corrections being turned off.

- $t\bar{t}$ +HF: A large conservative uncertainty of 50% is assumed for each the tt+bb and tt+cc cross section. The 50% on the ttbb rate is the leading uncertainty in the analysis. The largest rate variations observed by Sherpa NLO parameter variations were 30%. Therefore, a cross check will be performed repeating the final results with a prior of 30%.

Systematic uncertainty on the ttcc contribution due to the choice of the MC generator is evaluated by comparing the Powheg+Pythia and Madgraph+Pythia simulations: These uncertainties come from the factorisation and renormalisation scale variations, matching threshold and c-quark mass variations in the Madgraph+Pythia ttbar simulation.

- Parton shower: To assess the uncertainties coming from the parton shower and the hadronisation model, the ttbar+light, tt+cc and tt+bb shapes and rates are estimated from Powheg+Herwig instead of Powheg+Pythia. This uncertainty is then implemented with three uncorrelated components, one per ttbar sub-sample.

QCD

Systematic uncertainties on the multijet background estimate via the Matrix Method receive contributions from the limited data statistics, particularly at high jet and

b-tag multiplicities, as well as from the uncertainty on the fake rates, estimated in different control regions. A combined conservative uncertainty of 50% due to all these effects is assigned, which is taken as correlated across jet and b-tag multiplicity bins, but uncorrelated between electron and muon channels.

A shape uncertainty is assigned to the fake multijets by varying the fake efficiencies up and down. Another shape uncertainty comes from shifting up and down by 10% the overall yield of all the MC samples subtracted from fake CR.

V+jets

The W/Z +jet contributions are obtained from the simulation and normalized to the inclusive NNLO cross section. A reweighting is applied to improve the modeling of the WZ boson p_T spectrum. The full difference between applying and not applying this reweighting is taken as a systematical uncertainty.

The V+jets cross section uncertainty in the 4jet bin is 48%, and another 24% are assigned for each the 5 jet and 6 jet events (ie. 3 nuisance parameters (NPs) for each the W+jets and Z+jets cross section).

ttH

The ttH cross section uncertainties are provided by the LHCXSWG [134]: +8.9%, −12.2%, which includes the contributions from uncertainties on α_s , PDF, and QCD scales.

$t\bar{t}V$

The cross section uncertainty is 30%. A shape uncertainty is assigned coming from a variation of the ISR, which is detailed in the $t\bar{t}H$ note [\[92\]](#).

VV

Uncertainty on the diboson backgrounds rate includes the uncertainty on the inclusive diboson NNLO cross section of 5% added in quadrature to the uncertainty of 24% for extrapolating to each 4, 5 and 6 jet events, ie. for 6 jet events the uncertainty has 3 NPs with priors of 24.5%, 24%, 24%.

single top

The cross section uncertainty is +5%, -4%, corresponding to the weighted average of the theoretical uncertainties on s-, t- and Wt-channel production.

An uncertainty on the single top background shape is assessed by comparing Wt-channel MC samples generated using different schemes to take into account Wt and $t\bar{t}$ diagrams interference.

5.7 Statistical method

Hypothesis testing is performed using a modified frequentist method as implemented in ROOSTATS [132]. It is based on the `profile likelihood` method, which implements the systematic uncertainties as nuisance parameters and fits (profiles) them to the data. This procedure minimizes the impact of systematic uncertainties on the search sensitivity by taking advantage of the high-statistics background-dominated control regions. The distributions of the final discriminants from each of the regions considered are combined into a statistical analysis to test for the presence of a signal at each value of the hypothesized Higgs boson mass, $m_{H^+} = 200, 225, 250, 275, 300, 350, 400, 450, 500, 550$ and 600 GeV.

Gaussian constraint terms are used. The fitted errors, $\Delta\alpha$, represent the posterior uncertainty in units of σ_α . Therefore, a value of $\Delta\alpha$ close to 1 indicates that the data does not yield any particular sensitivity to the systematic uncertainty and the uncertainty is constrained by its prior term. Conversely, a value of $\Delta\alpha$ much smaller than 1 indicates sufficient sensitivity in the data to constrain the nuisance parameter more strongly than the prior uncertainty.

The signal event rate is controlled by the parameter of interest μ , where $\mu = 1$ corresponds to the observed signal strength being equal to the theory expectation. In order to be model independent, the signal is normalized to a cross section of 1 pb. The simulated distribution is described using a probability density function f_i . Let n be the number of observed events and let m be the number of expected events. Thus, the expected and observed number of events in each bin i is $m_i = mf_i$ and n_i , respectively. Introducing the

nuisance parameters $\boldsymbol{\theta}$ and k control regions, the resulting likelihood is given by:

$$\mathcal{L}(\mu) = \prod_k \prod_{l_k} \text{Poisson}(n_{l_k}|m_{l_k}) \prod_i \text{Poisson}(n_i|m_i) \prod_j p(\tilde{\theta}_j|\theta_j), \quad (5.2)$$

where the indices, i (signal region) and l_k (control region k), indicate the bin of the BDT distribution. Nuisance parameters, $\boldsymbol{\theta}$, are used to describe the effect of the systematic uncertainties while $p(\tilde{\theta}_j|\theta_j)$ are the Gaussian constraints relating each parameter to its nominal estimate $\tilde{\theta}_j$. We perform a profile likelihood statistical analysis with μ as the parameter of interest and $\boldsymbol{\nu}$ as additional nuisance parameters that are constrained by data in the control and signal regions. Note that m is a function of all the parameters, hence $m \equiv m(\mu, \boldsymbol{\nu}, \boldsymbol{\theta})$. The test statistic is given by [133]:

$$q_\mu = -2 \log \frac{\mathcal{L}(\mu, \hat{\hat{\boldsymbol{\theta}}}_\mu, \hat{\hat{\boldsymbol{\nu}}}_\mu)}{\mathcal{L}(\hat{\mu}, \hat{\boldsymbol{\theta}}, \hat{\boldsymbol{\nu}})}, \quad 0 \leq \hat{\mu} \leq \mu, \quad (5.3)$$

where $\hat{\hat{\boldsymbol{\theta}}}_\mu$ and $\hat{\hat{\boldsymbol{\nu}}}_\mu$ are the maximum likelihood estimators (MLE) of the nuisance parameters for a fixed μ , while $\hat{\boldsymbol{\theta}}$, $\hat{\boldsymbol{\nu}}$ and $\hat{\mu}$ are the global MLEs of $\boldsymbol{\theta}$, $\boldsymbol{\nu}$ and μ , respectively. The limit itself is derived using the CLs criterion [129] and asymptotic approximations [133]. For the calculation of the expected limits and the error bands, the Asimov data set [133] is employed.

5.7.1 Histogram Treatment

To reduce the impact of limited statistics on the fit results, the raw inputs undergo a certain procedure. This is the same procedure as used in the $t\bar{t}H \rightarrow t\bar{t}b\bar{b}$ analysis [92], in particular the same smoothing algorithm has been used.

- H_T^{Had} variable is binned non-uniformly, such that in each bin there is enough data statistics. This binning depends on the category. The BDT output variable is also binned non uniformly, with a wide bin at each the beginning and the end of the spectrum, to catch enough data statistics. The binning of the BDT histograms is mass-dependent. Typically the final histograms have 15-20 bins. The non-uniformly binned input histograms are refilled into histograms with equidistant binning in order to be used inside ROOT `HistFactory`.
- Systematic uncertainties which are not derived by applying a weight, are smoothed. The smoothing algorithm is applied only to the systematic variations, not the nominal histograms. The idea hereby is that bin-by-bin fluctuations result from statistical fluctuations. Therefore, the algorithm first iteratively rebins the effect of the systematic variation with a given threshold (start threshold chosen to be 8 %, which is halved per rebinning step), as long as the number of counted slope changes becomes less than a certain number (chosen to equal 3). However, the rebinned histogram is not returned, instead the bin contents are transferred to the histogram of the original binning (15 non-uniform bins). Then, this histogram is smoothed using the ROOT histogram `Smooth()` routine.
- Finally, the very small uncertainties are pruned, for a given process and a given category: If the change of the total rate is less than 0.5%, then this uncertainty does not act anymore on the rate. And if there is not a single bin where the rate changes by more than 0.5%, then this uncertainty acts no longer on the shape.

5.8 Results

The HF BDT output is used as final discriminant in the signal region, and in the four control regions H_T^{Had} is the discriminant. The control regions are always fit simultaneously with the signal region. The electron and muon channels are summed up to gain statistics, and in tests it was shown that a separation doesn't improve the limits significantly. The only asymmetry between electron and muon channel is expected in the QCD background, all other processes are symmetric with respect to the lepton flavour.

A binned maximum likelihood fit to the data is performed simultaneously in the five event categories, and each mass hypothesis is tested separately. The inputs to the simultaneous fit are the distributions of H_T^{Had} in the four CR, and the BDT output histograms in the SR. The procedures for quantifying how well the data agree with the background-only hypothesis and for determining exclusion limits are based on the profile likelihood ratio test [128]. The parameter of interest is the production cross section $\sigma(gb \rightarrow tH^+)$ multiplied by the branching fraction $\text{BR}(H^+ \rightarrow tb)$, also referred to as the signal strength. All systematic uncertainties, either from theoretical or experimental sources, are implemented as nuisance parameters with log-normal constraint terms. The largest uncertainties for any tested mass point are those arising from the modelling of the $t\bar{t}$ processes. For $m_{H^+} < 350$ GeV, the uncertainty on the $t\bar{t}+b\bar{b}$ cross section has the largest impact on the result. For higher-mass hypotheses, the uncertainties on the shape of the distributions for $t\bar{t}+b\bar{b}$ from the reweighting to the NLO prediction are dominant. The uncertainties decrease for higher-mass hypotheses because of the larger signal acceptance and the improved separation between signal and background of the BDT. The pulls of the nuisance parameters after profiling to the data are almost all within $\pm 1\sigma$ and never exceed $\pm 1.5\sigma$.

for all tested mass hypotheses. The pulls that are larger than $\pm 1\sigma$ in at least one of the tested mass hypotheses are those associated with uncertainties on the $t\bar{t}$ +HF cross sections, on the parton shower modelling of the $t\bar{t}$ + $c\bar{c}$ process, and on the $t\bar{t}$ + $b\bar{b}$ NLO modelling, derived from variations of the functional form of the renormalisation scale.

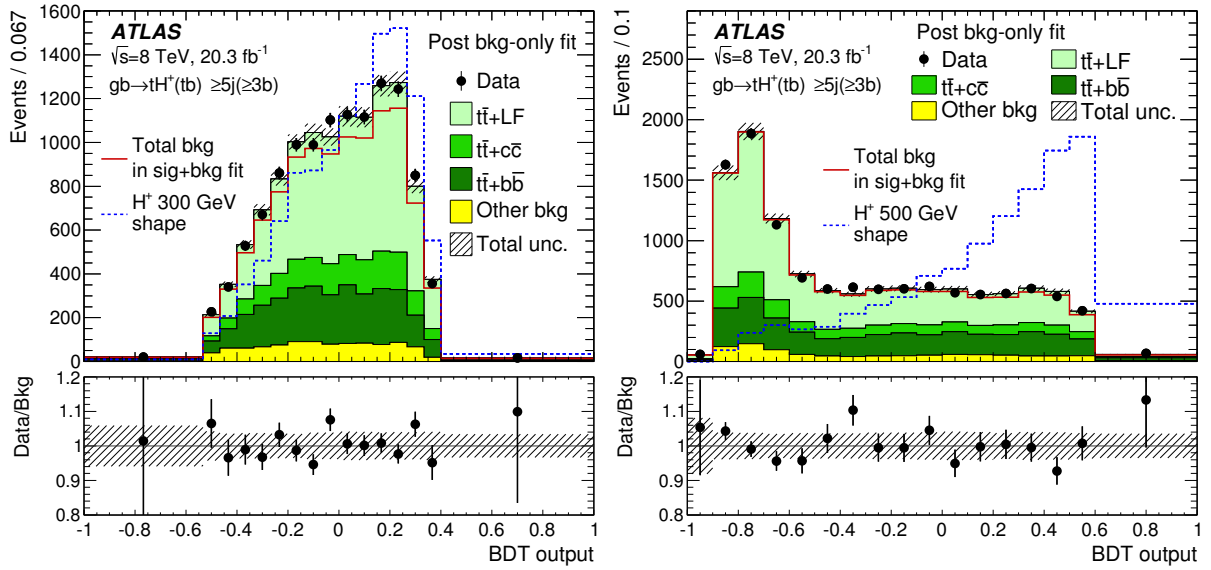


Figure 5.18: Distributions of the BDT output in the signal-rich region after the fit to the data under the background-only hypothesis. The BDT was trained for two signal mass hypotheses: (a) 300 GeV and (b) 500 GeV. Each background is normalised according to its post-fit cross section. The solid red line shows the total background after an unconditional fit under the background-plus-signal hypothesis with a signal mass of (a) 300 GeV and (b) 500 GeV. The signal shape is shown as a superimposed dashed blue line normalised to the data. The hatched bands show the post-fit uncertainties taking into account the constraints and correlations of the nuisance parameters. The lower panels display the ratio of the data to the total predicted background.

The modified frequentist method (CLs) [129] and asymptotic formulae [130] are used to calculate upper limits on $\sigma(gb \rightarrow tH^+) \times \text{BR}(H^+ \rightarrow tb)$. The 95% confidence level (CL) upper limits are presented in figure 5.19. The mass hypotheses are tested in 25 GeV

steps between 200 and 300 GeV, and in 50 GeV steps up to 600 GeV. At 250 GeV, the local p_0 -value for the observation to be in agreement with the background-only hypothesis reaches its smallest value of 0.9% (corresponding to 2.4 standard deviations). At m_{H^\pm} values of 300 and 450 GeV, the excess of the data with respect to the background-only hypothesis corresponds to 2.3 standard deviations.

The expected upper limit is computed with a signal injected at $m_{H^\pm} = 300$ GeV, with a production cross section times branching fraction of 1.65 pb, corresponding to the best-fit value of the signal strength at this mass point. This results in an excess that is more localised at the injected mass value, i.e. extends less to lower and higher masses than the trend seen in the observed upper limit, as shown in figure 5.19. The H^\pm signal is generated with a zero width. The experimental mass resolution is approximately 50 GeV for the mass hypothesis of 300 GeV. A systematic background mismodelling is considerably more likely to give rise to the observed excess than a hypothesised signal at a specific mass. The cross sections of the $t\bar{t}$ +HF backgrounds and the shape of the $t\bar{t}+b\bar{b}$ component have large uncertainties which are correlated with the signal normalisation. Together with the pre-fit excess of data compared to the SM prediction, this can result in a post-fit excess over a wide H^\pm mass range. The fits were repeated using two alternative, less sensitive, discriminants in the SR: (a) a BDT trained against the sum of all backgrounds or (b) the variable H_T^{Had} . Similar excesses were observed with these two alternative methods.

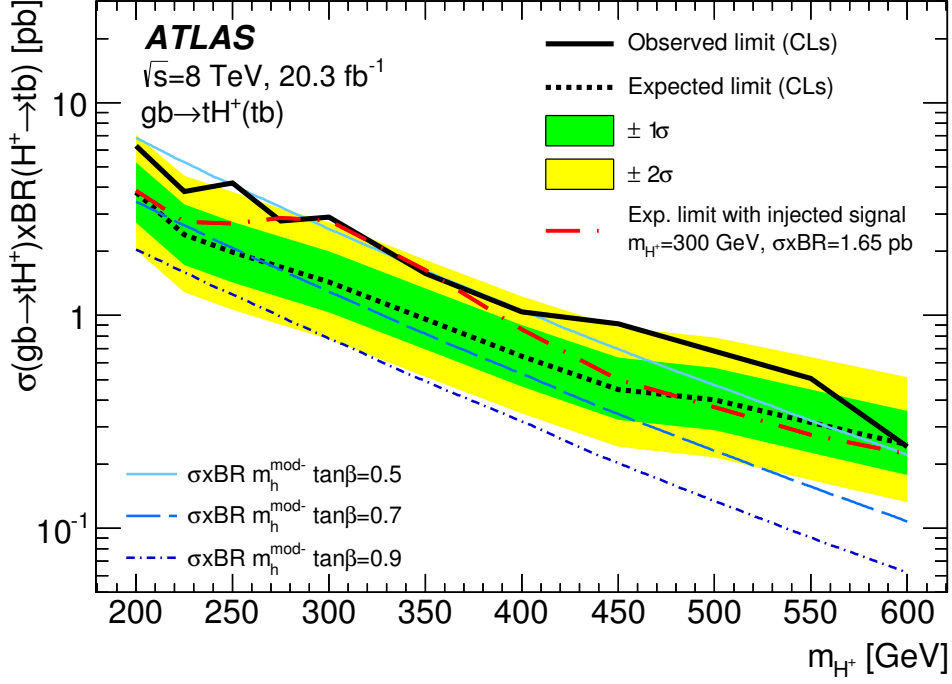


Figure 5.19: Expected and observed limits for the production of $H^{\pm} \rightarrow tb$ in association with a top quark, as well as bands for 68% (in green) and 95% (in yellow) confidence intervals. The red dash-dotted line shows the expected limit obtained in the case where a simulated signal is injected at $m_{H^{\pm}} = 300$ GeV, with a production cross section times branching fraction of 1.65 pb (corresponding to the best-fit signal strength at that mass hypothesis), yielding a deviation from the expectation that extends less to higher and lower mass values than the observed upper limit.

Chapter 6

Conclusion

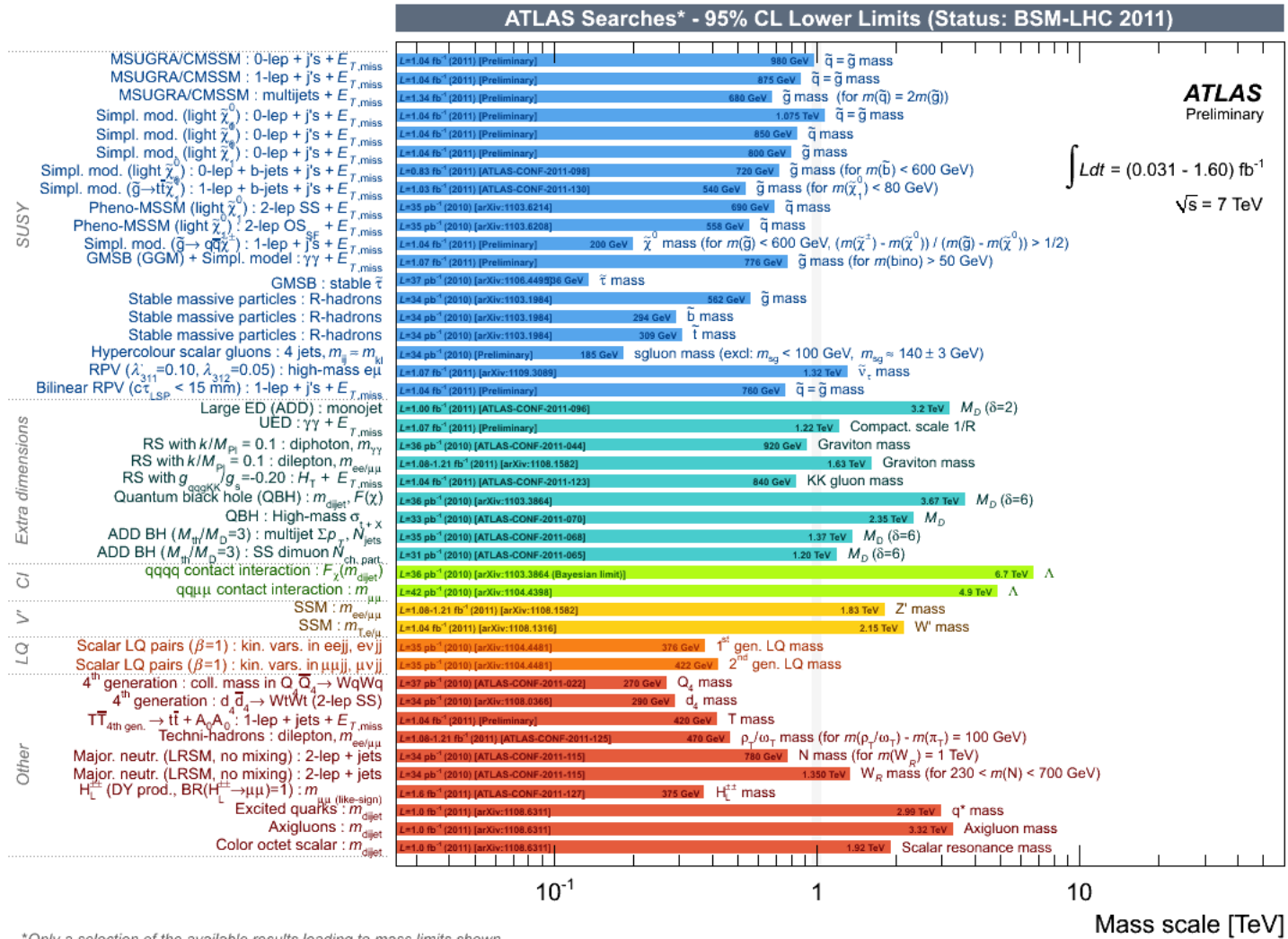
“What we observe is not nature itself, but nature exposed to our method of questioning”

– Werner Heisenberg

There are great deal of unanswered questions in particle physics, which can not be explained by the Standard Model and that require extensions to it. Among these are questions regarding gravity, unification of fundamental forces and the origin of dark matter and energy. One possible extension for BSM physics is SUSY. Introducing this would at least double the particle spectrum and would lead to five Higgs bosons, of which three are neutral and two are charged.

Although there is still no confirmation for BSM phenomena, the search is on full throttle. A glance at figure [6.1](#) shows the extent of such searches performed solely in the ATLAS collaboration. One must not look at these results as failures of discovery, but rather as steps toward a much clearer understanding of the universe. It is this curiosity driven approach, that should always guide our scientific path.

Figure 6.1: A selection of Run-I results obtained by the ATLAS experiment in search for new discoveries. In blue, searches for various supersymmetric models, in turquoise, models involving extra dimensions, and the other colors showing even more exotic models.



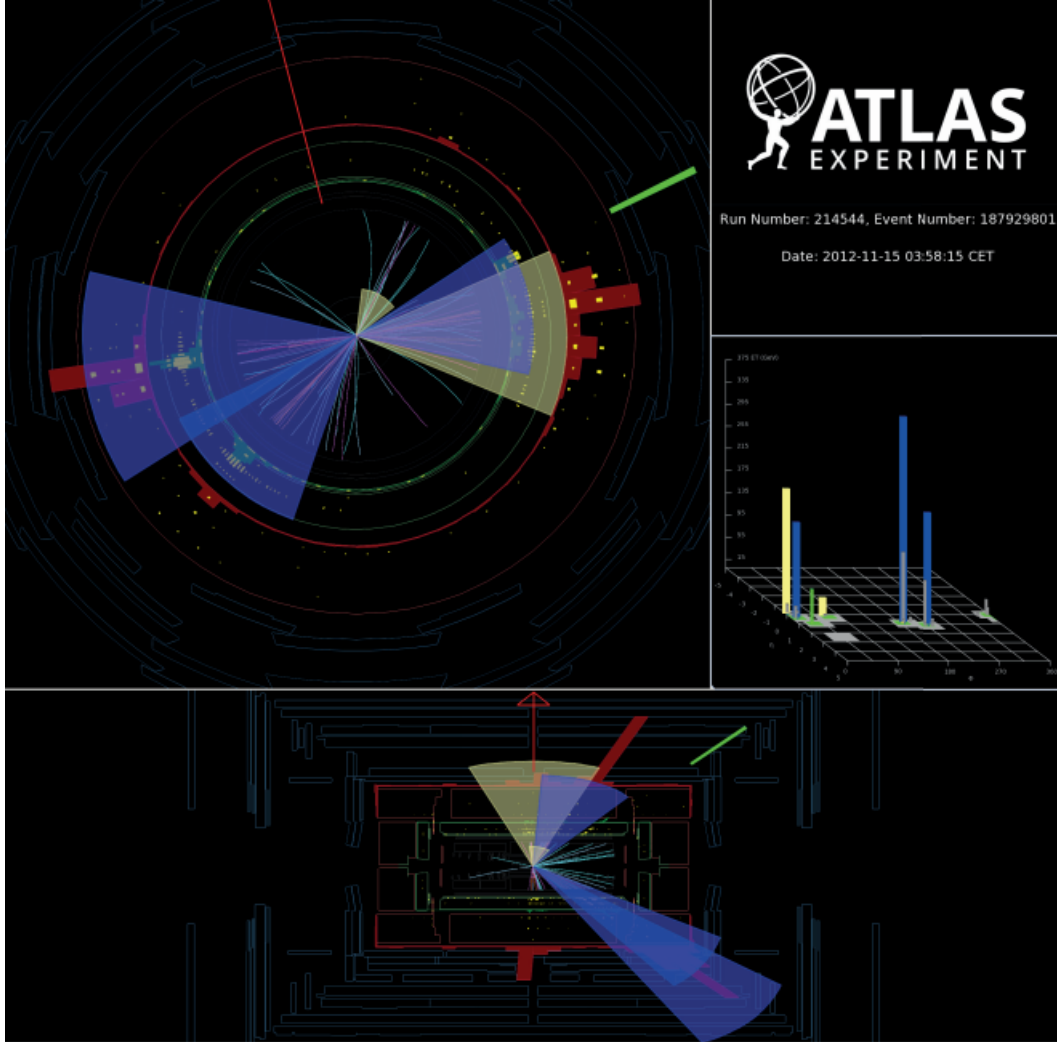


Figure 6.2: Event display of one event from the signal-rich region in the search for $gb \rightarrow tH^\pm$ with $H^\pm \rightarrow tb$. The run number is 214544, and the event number is 187929801. This event has five jets (displayed as yellow and blue cones) including three b-tagged jets (blue cones) and an electron (green line). The red line displays the direction of the missing transverse momentum. The two-dimensional histogram displays the energy deposits of the objects as a function of η and ϕ as calculated from the calorimeter cells.

Bibliography

- [1] ATLAS Collaboration, *Observation of a new particle in the search for the Standard Model Higgs boson with the ATLAS detector at the LHC*, Phys. Lett. B 716 (2012) 1, arXiv: 1207.7214 [hep-ex].
- [2] CMS Collaboration, *Observation of a new boson at a mass of 125 GeV with the CMS experiment at the LHC*, Phys. Lett. B 716 (2012) 30, arXiv: 1207.7235 [hep-ex].
- [3] ATLAS and CMS Collaborations, *Combined measurement of the Higgs boson mass in pp collisions at $\sqrt{s} = 7$ and 8 TeV with the ATLAS and CMS experiments*, Phys. Rev. Lett. 114 (2015) 191803, arXiv: 1503.07589 [hep-ex].
- [4] Particle Data Group, *Review of Particle Physics (RPP)*
- [5] S. L. Glashow, *Partial-symmetries of weak interactions*, Nuclear Physics 22 (1961) no. 4, 579 - 588
- [6] S. Weinberg, *A Model of Leptons*, Phys. Rev. Lett. 19 (Nov, 1967) 1264-1266
- [7] A. Salam, *Weak and Electromagnetic Interactions*, Conf.Proc. C680519 (1968) 367-377

- [8] D. Decamp and Alexander Finch et al., The ALEPH collaboration, *Determination of the number of light neutrino species*, Physics Letters B 231 (1989) no. 4, 519 - 529
- [9] LHCb Collaboration, *Observation of $J/\psi p$ resonances consistent with pentaquark states in $\Lambda_b^0 \rightarrow J/\psi K^- p$ decays*, Phys. Rev. Lett. 115, 072001 (2015), arXiv: 1507.3414 [hep-ex].
- [10] M. Karliner and H. J. Lipkin, *A diquark - triquark model for the KN pentaquark*, Phys. Lett. B575 (2003) 249, arXiv:hep-ph/0402260.
- [11] UA1 Collaboration, *Experimental observation of isolated large transverse energy electrons with associated missing energy at $\sqrt{s} = 540\text{GeV}$* , Physics Letters B 122 (1983) no. 1, 103 - 116
- [12] UA2 Collaboration, *Observation of single isolated electrons of high transverse momentum in events with missing transverse energy at the CERN pp collider*, Physics Letters B 122 (1983) no. 5-6, 476 - 485
- [13] UA1 Collaboration, *Experimental observation of lepton pairs of invariant mass around $95\text{GeV}/c^2$ at the CERN SPS collider*, Physics Letters B 126 (1983) no. 5, 398 - 410
- [14] UA2 Collaboration, *Evidence for $Z^0 \rightarrow e^+e^-$ at the CERN pp collider*, Physics Letters B 129 (1983) no. 1-2, 130 - 140
- [15] P. W. Higgs, *Broken symmetries, massless particles and gauge fields*, Phys.Lett. 12 (1964) 132 - 133

- [16] P. W. Higgs, *Broken Symmetries and the Masses of Gauge Bosons*, Phys. Rev. Lett. 13 (Oct, 1964) 508-509
- [17] Goldstone, J (1961). *Field Theories with Superconductor Solutions*. Nuovo Cimento 19: 154-164
- [18] F. Mandl and G. Shaw, *Quantum field theory*, A Wiley-Interscience publication. J. Wiley, 1993
- [19] J. F. Gunion et al., *The Higgs Hunter's Guide*, vol. 80. 2000
- [20] N. Arkani-Hamed, S. Dimopoulos, and G. Dvali, *The hierarchy problem and new dimensions at a millimeter*, Physics Letters B 429 (1998) no. 3-4, 263 - 272
- [21] Planck Collaboration, *Planck 2013 results. I. Overview of products and scientific results*, arXiv e-prints (Mar., 2013) , arXiv:1303.5062
- [22] G. Karagiorgi et al., *Leptonic CP violation studies at MiniBooNE in the $(3+2)$ sterile neutrino oscillation hypothesis*, Phys. Rev. D 75 (Jan, 2007) 013011
- [23] L. Canetti, M. Drewes, and M. Shaposhnikov, *Matter and antimatter in the universe*, New Journal of Physics 14 (2012) no. 9, 095012.
- [24] A. O. Sushkov et al., *New Experimental Limits on Non-Newtonian Forces in the Micrometer Range*, Phys. Rev. Lett. 107 (Oct, 2011) 171101
- [25] M. E. Peskin, *Beyond the Standard Model*, arXiv:hep-ph/9705479.

- [26] M. Maniatis, A. von Manteuffel, O. Nachtmann, *On the phenomenology of a two-Higgs-doublet model with maximal CP symmetry at the LHC*, arXiv:1009.1869 [hep-ph]
- [27] The ATLAS Collaboration, *The ATLAS Experiment at the CERN Large Hadron Collider*, JINST 3 (2008).
- [28] G. C. Branco, P. M. Ferreira, L. Lavoura, M. N. Rebelo, Marc Sher, Joao P. Silva, *Theory and phenomenology of two-Higgs-doublet models*, arXiv:1106.0034 [hep-ph]
- [29] The ATLAS Collaboration, *Search for charged Higgs bosons decaying via $H \rightarrow \tau\nu$ in top quark pair events using pp collision data at $\sqrt{s} = 7\text{TeV}$ with the ATLAS detector*, JHEP 1206 (2012) 039
- [30] M. S. Carena and H. E. Haber, *Higgs boson theory and phenomenology*, Prog.Part.Nucl.Phys. 50 (2003) 63-152, arXiv:hep-ph/0208209
- [31] C. Bernaciak et al., *Fox-Wolfram Moments in Higgs Physics*, Phys. Rev. D 87.7 (2013) 073014, arXiv: 1212.4436 [hep-ph]
- [32] A. Djouadi, *The Anatomy of electro-weak symmetry breaking. I: The Higgs boson in the Standard Model*, Phys.Rept. 457 (2008) 1-216,
- [33] D. J. Warner, *Project study for a new 50 MeV linear accelerator for the C. P. S*, Tech. Rep. CERN-MPS-LINP-73-1, CERN, Geneva, Oct, 1973.
- [34] N. Angert et al., *CERN heavy-ion facility design report*. CERN, Geneva, 1993.
- [35] L. Arnaudon and et al., *Linac4 Technical Design Report*, Tech. Rep. CERN-AB-2006-084. CARE-Note-2006-022-HIPPI, CERN, Geneva, Dec, 2006.

- [36] C. Lef  vre, *The CERN accelerator complex*. du CERN, Dec, 2008.
- [37] K. Hanke, *Past and present operation of the CERN PS Booster*, Int. J. Mod. Phys. A 28 (2013) 1330019. 25 p.
- [38] M. Grieser et al., *Storage ring at HIE-ISOLDE*, The European Physical Journal Special Topics 207 (2012) no. 1, 1-117
- [39] G. Plass, *The CERN proton synchrotron: 50 years of reliable operation and continued development*, The European Physical Journal H 36 (2012) no. 4, 439-454.
- [40] L. Evans and P. Bryant, *LHC Machine*, JINST 3 (2008) .
- [41] *The LHC Ring with experiments* http://lhc-machine-outreach.web.cern.ch/lhc-machine-outreach/lhc_in_pictures.htm.
- [42] The ALICE Collaboration, *The ALICE experiment at the CERN LHC*, JINST 3 (2008).
- [43] The CMS Collaboration, *The CMS experiment at the CERN LHC*, JINST 3 (2008).
- [44] The LHCb Collaboration, *The LHCb Detector at the LHC*, JINST 3 (2008) .
- [45] E. Prebys, *Bunch Spacing and Pileup in High Energy Hadron Colliders*.
- [46] ATLAS Collaboration, *ATLAS detector and physics performance: Technical Design Report*, Technical Design Report ATLAS. CERN, Geneva, 1999. <https://cdsweb.cern.ch/record/391176>

- [47] ATLAS Collaboration, *Studies of the performance of the ATLAS detector using cosmic-ray muons*, The European Physical Journal C - Particles and Fields 71 (2011) 1-36. <http://dx.doi.org/10.1140/epjc/s10052-011-1593-6>
- [48] ATLAS Collaboration, *The ATLAS Inner Detector commissioning and calibration*, The European Physical Journal C - Particles and Fields 70 (2010) 787-821. <http://dx.doi.org/10.1140/epjc/s10052-010-1366-7>.
- [49] ATLAS Collaboration, *ATLAS inner detector: Technical Design Report 1. Technical Design Report ATLAS*. CERN, Geneva, 1997. <https://cdsweb.cern.ch/record/331063>.
- [50] ATLAS Collaboration, *ATLAS inner detector: Technical Design Report, 2. Technical Design Report ATLAS*. CERN, Geneva, 1997. <https://cdsweb.cern.ch/record/331064>.
- [51] ATLAS Collaboration, *ATLAS pixel detector: Technical Design Report. Technical Design Report ATLAS*. CERN, Geneva, 1998. <https://cdsweb.cern.ch/record/381263>.
- [52] ATLAS Collaboration, *ATLAS pixel detector electronics and sensors*, JINST 3 (2008) P07007.
- [53] ATLAS Collaboration, *The barrel modules of the ATLAS semiconductor tracker* , Nucl.Instrum.Meth. A568 (2006) 642-671
- [54] ATLAS Collaboration, *The ATLAS semiconductor tracker end-cap module*, Nucl.Instrum.Meth. A575 (2007) 353-389

- [55] ATLAS Collaboration, *The Silicon microstrip sensors of the ATLAS semiconductor tracker* , Nucl.Instrum.Meth. A578 (2007) 98-118
- [56] The ATLAS TRT Collaboration, *The ATLAS TRT barrel detector* , JINST 3 (2008) P02014.
- [57] The ATLAS TRT Collaboration, *The ATLAS TRT end-cap detectors*, JINST 3 (2008) P10003.
- [58] The ATLAS TRT Collaboration, *The ATLAS Transition Radiation Tracker (TRT) proportional drift tube: Design and performance*, JINST 3 (2008) P02013.
- [59] ATLAS Collaboration, *ATLAS central solenoid: Technical Design Report*. Technical Design Report ATLAS. CERN, Geneva, 1997. <https://cdsweb.cern.ch/record/331067>.
- [60] ATLAS Collaboration, *ATLAS calorimeter performance: Technical Design Report*. Technical Design Report ATLAS. CERN, Geneva, 1996. <https://cdsweb.cern.ch/record/331059>.
- [61] ATLAS Collaboration, *ATLAS liquid-argon calorimeter: Technical Design Report*. Technical Design Report ATLAS. CERN, Geneva, 1996. <https://cdsweb.cern.ch/record/331061>.
- [62] ATLAS Collaboration, *ATLAS tile calorimeter: Technical Design Report*. Technical Design Report ATLAS. CERN, Geneva, 1996. <https://cdsweb.cern.ch/record/331062>.

- [63] ATLAS Collaboration, *ATLAS muon spectrometer: Technical Design Report*. Technical Design Report ATLAS. CERN, Geneva, 1997. <https://cdsweb.cern.ch/record/331068>.
- [64] ATLAS Collaboration, *ATLAS barrel toroid: Technical Design Report*. Technical Design Report ATLAS. CERN, Geneva, 1997. <https://cdsweb.cern.ch/record/331065>.
- [65] ATLAS Collaboration, *ATLAS end-cap toroids: Technical Design Report*. Technical Design Report ATLAS. CERN, Geneva, 1997. <https://cdsweb.cern.ch/record/331066>.
- [66] ATLAS Collaboration, *Muon reconstruction efficiency in reprocessed 2010 lh proton-proton collision data recorded with the atlas detector*. ATLAS-CONF-2011-063.
- [67] ATLAS Collaboration, *A measurement of the muon reconstruction efficiency in 2010 atlas data using j/ψ decays*. ATLAS-CONF-2012-125.
- [68] <https://twiki.cern.ch/twiki/bin/viewauth/AtlasProtected/MCPAnalysisGuidelinesData2012>.
- [69] GEANT4 Collaboration, S. Agostinelli et al., *GEANT4 - A Simulation Toolkit*, Nucl. Instr. and Meth. A506 (2003) 250.
- [70] *Improved luminosity determination in pp collisions at $\sqrt{s} = 7$ TeV using the ATLAS detector at the LHC (2013)*, arXiv: 1302.4393 [hep-ex].

- [71] P. Barnreuther, M. Czakon and A. Mitov, *Percent Level Precision Physics at the Tevatron: First Genuine NNLO QCD Corrections to $q\bar{q} \rightarrow t\bar{t}$* , Phys. Rev. Lett. 109 (2012) 132001.
- [72] M. Czakon and A. Mitov, *NNLO corrections to top-pair production at hadron colliders: the all-fermionic scattering channels*, JHEP 1212 (2012) 054.
- [73] M. Czakon and A. Mitov, *NNLO corrections to top pair production at hadron colliders: the quark-gluon reaction*, JHEP 1301 (2013) 080.
- [74] M. Czakon, P. Fiedler and A. Mitov, *The total top quark pair production cross-section at hadron colliders through $O(\alpha_S^4)$ 2013*, <http://arxiv.org/abs/1303.6254>.
- [75] M. Czakon and A. Mitov, *Top++: a program for the calculation of the top-pair cross-section at hadron colliders (2011)*, <http://arxiv.org/abs/1112.5675>.
- [76] A. Martin et al., *Parton distributions for the LHC*, Eur. Phys. J. C 63 (2009) 189, <http://arxiv.org/abs/0901.0002>.
- [77] A. Martin et al., *Uncertainties on α_S in global PDF analyses and implications for predicted hadronic cross sections*, Eur. Phys. J. C 64 (2009) 653, <http://arxiv.org/abs/0905.3531>.
- [78] J. Gao et al., *The CT10 NNLO global analysis of QCD (2013)*, <http://arxiv.org/abs/1302.6246>.
- [79] R. Ball et al., *Parton distributions with LHC data (2012)*, <http://arxiv.org/abs/1207.1303>.

- [80] M. Aliev et al., *HATHOR: HAdronic Top and Heavy quarks crOss section calculator*, JComput. Phys. Commun. 182 (2011) 1034, <http://arxiv.org/abs/1007.1327>.
- [81] *Measurement of the top quark pair production cross section in the single-lepton channel with ATLAS in proton-proton collisions at 8 TeV using kinematic fits with b-tagging*, ATLAS-CONF-2012-149.
- [82] *Measurement of the jet multiplicity in top-anti-top final states produced in 7 TeV proton-proton collisions with the ATLAS detector*, ATLAS-CONF-2012-155 (2012).
- [83] M. Botjet et al. *The PDF4LHC Working Group Interim Recommendations (2011)* <http://arxiv.org/abs/1101.0538>.
- [84] P. M. Nadolsky et al. *Implications of CTEQ global analysis for collider observables* Phys. Rev. D 78 (2008) 013004.
- [85] N. Kidonakis., *Next-to-next-to-leading-order collinear and soft gluon corrections for t-channel single top quark production*, Phys. Rev. D 83 (2011) 091503, <http://arxiv.org/abs/1103.2792>.
- [86] N. Kidonakis., *NNLL resummation for s-channel single top quark production* Phys. Rev. D 81 (2010) 054028, <http://arxiv.org/abs/1001.5034>.
- [87] N. Kidonakis., *Two-loop soft anomalous dimensions for single top quark associated production with a W^- or H^-* Phys. Rev. D 82 (2010) 054018, <http://arxiv.org/abs/1005.4451>.
- [88] S. Frixione et al., *Single-top production in MC@NLO*, JHEP 0603 (2006) 092, <http://arxiv.org/abs/hep-ph/0512250>.

- [89] M. L. Mangano, M. Moretti, F. Piccinini, R. Pittau, and A. D. Polosa., *ALPGEN, a generator for hard multiparton processes in hadronic collisions*, JHEP 07 (2003) 001.
- [90] *Monte Carlo samples used for top physics*, ATL-PHYS-INT-2010-132, 2010.
- [91] K. Melnikov and F. Petriello., *Electroweak gauge boson production at hadron colliders through $O(\alpha_s^2)$* , <http://arxiv.org/abs/0609070>.
- [92] The ATLAS collaboration., *Search for the Standard Model Higgs boson produced in association with top quarks in pp collisions at $\sqrt{s} = 8$ TeV with the ATLAS detector at the LHC*, ATLAS-COM-PHYS-2013-1659, 2013.
- [93] G. Corcella et al., *HERWIG 6: an event generator for hadron emission reactions with interfering gluons (including supersymmetric processes)*, <http://dx.doi.org/10.1088/1126-6708/2001/01/010>.
- [94] J. Campbell and R. Ellis., *An update on vector boson pair production at hadron colliders*, arXiv: 9905386 (hep-ph).
- [95] G. Bevilacqua et al., *HELAC-NLO*, <http://arxiv.org/abs/1110.1499v2>.
- [96] P. Nason., *A new method for combining NLO QCD with shower Monte Carlo algorithms*, 11 (2004) 040.
- [97] S. Alioli et al., *A general framework for implementing NLO calculations in shower Monte Carlo programs: the POWHEG BOX*, <http://arxiv.org/abs/1002.2581>.
- [98] S. Dittmaier et al., *Handbook of LHC Higgs Cross Sections: 1. Inclusive Observables (2011)*, <http://arxiv.org/abs/1101.0593>.

- [99] <https://twiki.cern.ch/twiki/bin/view/AtlasProtected/TopCommonParametersMC12>.
- [100] Z. Was and P. Golonka., *TAUOLA as tau Monte Carlo for future applications*, Nucl. Phys. Proc. Suppl. 144 (2005) 88, <http://arxiv.org/abs/hep-ph/0411377>.
- [101] E. Barberio, B. van Eijk and Z. Was., *PHOTOS: A universal Monte Carlo for QED radiative corrections in decays*, Comput. Phys. Commun. 66 (1991) 115.
- [102] P. Z. Skands., *Tuning Monte Carlo Generators: The Perugia Tunes*, Phys. Rev. D 82 (2010) 074018, <http://arxiv.org/abs/1005.3457>.
- [103] *ATLAS tunes of PYTHIA 6 and Pythia 8 for MC11*, ATL-PHYS-PUB-2011-009.
- [104] *New ATLAS event generator tunes to 2010 data*, ATL-PHYS-PUB-2011-008.
- [105] *Electron performance measurements with the ATLAS detector using the 2010 LHC proton-proton collision data*, Eur. Phys. J. C 72 (2012) 1909, <http://arxiv.org/abs/1110.3174>.
- [106] W. Lampl et al., *Calorimeter clustering algorithms: description and performance*, ATL-LARG-PUB-2008-002.
- [107] J Hartert and I Ludwig., *Electron isolation in the ATLAS experiment*, ATL-PHYS-INT-2010-052.
- [108] [SVN:root/Reconstruction/egamma/egammaAnalysis/egammaAnalysisUtils](#).
- [109] G. S. M. Cacciari and G. Soyez., *The anti- $k(t)$ jet clustering algorithm*, JHEP 0804 (2008) 063, <http://arxiv.org/abs/0802.1189>.

- [110] M. Cacciari and G. P. Salam., *Dispelling the N^3 myth for the $k(t)$ jet-finder*, Phys. Lett. B 641 (2006) 57, <http://arxiv.org/abs/hep-ph/0512210>.
- [111] The ATLAS Collaboration., *Local hadronic calibration*, ATL-LARG-PUB-2009-001.
- [112] *Hadronic calibrations of the ATLAS liquid argon end-cap calorimeter in the pseudorapidity region $1.6 < |\eta| < 1.8$ in beam tests*, , Nucl. Instr. Meth. A 531 (1986) 1896.
- [113] M. Cacciari, G. P. Salam and G. Soyez., *The catchment area of jets*, JHEP 0804 (2008) 005, <http://arxiv.org/abs/0802.1188>.
- [114] *Pile-up subtraction and suppression for jets in ATLAS*, ATLAS-CONF-2013-083.
- [115] The ATLAS collaboration., *Commissioning of the ATLAS high-performance b -tagging algorithms in the 7 TeV collision data*, ATLAS-CONF-2011-102, 2011.
- [116] <https://twiki.cern.ch/twiki/bin/view/AtlasProtected/ExtendedPileupRewighting>.
- [117] A. Hoecker, P. Speckmayer, J. Stelzer, J. Therhaag, E. von Toerne, and H. Voss, “TMVA: Toolkit for Multivariate Data Analysis,” PoS A CAT 040 (2007) [physics/0703039].
- [118] ATLAS Collaboration, *Object selection and calibration, background estimation and MC samples for the Winter 2013 top quark analyses with 2012 data*, 2013, ATLAS-COM-2013-088.

- [119] *Luminosity determinatino in pp collisions at $\sqrt{s} = 7$ TeV using the ATLAS detector at the LHC*, Eur. Phys. J C71 (2011) 1630, <http://arxiv.org/abs/1101.2185>.
- [120] *Jet energy measurement with the ATLAS detector in proton-proton collisions at $\sqrt{s} = 7$ TeV*, (2011), <http://arxiv.org/abs/1112.6426>.
- [121] ATLAS Collaboration , *In-situ jet energy scale and jet schape corrections for multiple interactions in the first ATALS data at the LHC (2011)*, eprint: <http://cdsweb.cern.ch/record/1337780>.
- [122] ATLAS Collaboration ., *In-situ pseudorapidity intercalibration for evaluationof jet energy scale uncertainty using dijet events in proton-proton collision at $\sqrt{s} = 7$ TeV*, (2011) eprint:, <http://cdsweb.cern.ch/record/1334876>.
- [123] ATLAS Collaboration , *Jet energy resolution and reconstruction efficiency from in-situ techniques with the ATLAS Detector Using Proton-Proton Collisions at the Center of Mass Energy $\sqrt{s} = 7$ TeV* (2011), eprint:, <http://cdsweb.cern.ch/record/1281311>.
- [124] ATLAS Collaboration , , *In-situ pseudorapidity intercalibration to evaluate jet en-ergy scale uncertainty and calorimeter performance in the forward region*, (2011), eprint: <http://cdsweb.cern.ch/record/1281312>.
- [125] ATLAS Collaboration , *Calibration of b-jets using dileptonic top pair events in a combinatorial likelihood approach with the ATALS experiment*, (2014) eprint: <http://cdsweb.cern.ch/record/1664335>.

- [126] ATLAS Collaboration , *b-jet tagging calibration on c-jets containing D^* meson*, (2014) eprint: <http://cdsweb.cern.ch/record/1435193>.
- [127] ATLAS Collaboration, *Measurement of the Mistag Rate of b-tagging algorithms with 5 fb^{-1} of Data Collected by the ATLAS Detector*, (2014) eprint: <http://cdsweb.cern.ch/record/1435194>.
- [128] ATLAS Collaboration , *Combined search for the Standard Model Higgs boson in pp collisions at $\sqrt{s} = 7\text{ TeV}$ with the ATLAS detector*, Phys. Rev. D 86 (2012) 032003, <http://arxiv.org/abs/1207.0319>.
- [129] A. L. Read , *Presentation of search results: the CLs 851 technique*, J. Phys. G28 (2002) 2693., <http://dx.doi.org/10.1088/0954-3899/28/10/313>.
- [130] G. Cowan et al. , *Asymptotic formulae for likelihood-based tests of new physics*, Eur. Phys. J. C 71 (2011) 1554, <http://arxiv.org/abs/1007.1727>.
- [131] M. Carena et al. , *MSSM Higgs Boson Searches at the LHC: Benchmark Scenarios after the 816 Discovery of a Higgs-like Particle*, Eur. Phys. J. C 73 (2013) 2552, <http://arxiv.org/abs/1302.7033>.
- [132] W. Verkerke and D. Kirkby , *The RooFit toolkit for data modeling*, User Manual, 2006, <http://roofit.sourceforge.net/docs/index.html>.
- [133] G. Cowan, K. Cranmer, E. Gross and O. Vitells , *Asymptotic formulae for likelihood-based tests of new physics*, Eur. Phys. J. C 71 (2011) 1554.
- [134] LHC Higgs Cross Section Working Group, <https://twiki.cern.ch/twiki/bin/view/LHCPhysics/LHCHXSWG>.

- [135] ATLAS Collaboration, *Search for charged Higgs bosons in the $H^\pm \rightarrow tb$ decay channel in pp collisions at $\sqrt{s} = 8$ TeV using the ATLAS detector*, <http://arxiv.org/abs/1512.03704>
- [136] G. D. Coughlan, J. E. Dodd, B. M. Gripaios, *The Ideas of Particle Physics: An Introduction for Scientists*, Cambridge University Press, 27 Jul 2006.

תקציר

תזה זו מציגה מחקר של חיפוש אחר בוזון היגס טעון בגלאי אטלס בעזרת התנגשויות פרוטון-פרוטון באנרגיית מרכז מסה של שבע ואחרי כן שמונה טרה-אלקטרון-וולט במאיץ החלקיקים LHC. המידע שנאסף במהלך שלש שנות הריצה הראשונות של המאיץ (2010-2012), נותח במטרה לחפש החלקיק בהנחה כי מסתו גבוהה ממסתו של הקווארק TOP. המחקר מכסה את תהליך היצירה באמצעות היתוך גלואן וקווארק מסוג BOTTOM לטובת יצירת בוזון היגס טעון אשר בתורו דועך לזוג קווארקים TOP, BOTTOM. על מנת להתמודד עם תהליכי רקע, שיטות של למידת מכונה יושמו על גבי הדמיות מונטה-קרלו של חלקיקים. גילוי של חלקיק זה יהווה סמן ברור עבור פיזיקה חדשה מעבר למודל הסטנדרטי של פיזיקת החלקיקים.

TEL AVIV UNIVERSITY

RAYMOND AND BEVERLY SACKLER
FACULTY OF EXACT SCIENCES
SCHOOL OF PHYSICS & ASTRONOMY



TEL AVIV
אוניברסיטת
תל אביב
UNIVERSITY

אוניברסיטת תל-אביב

הפקולטה למדעים מדויקים
ע"ש ריימונד ובברלי סאקלר
בית הספר לפיסיקה ואסטרונומיה

חיפוש אחר בוזון היגס טעון בגלאי אטלס במאיץ ההדרונים הגדול

הדר כהן

חיבור מדעי המוגש כחלק מדרישות התואר "מוסמך אוניברסיטה" במחלקה
לאנרגיות גבוהות באוניברסיטת תל אביב תחת הדרכת פרופסור **ארז עציון**.

אוקטובר 2016
Hadar.Cohen@cern.ch